Appendix B

Options

B.1 Proton Driver

B.1.1 Increasing Power to 2 or 4 MW

With an increased superconducting linac energy, the proton intensity could be increased by a factor of two (from 1×10^{14} to 2×10^{14}.) A further increase of a factor of two in average proton power could be achieved by adding a 24 GeV storage ring and operating the AGS at 5 Hz. An upgrade to 4 MW beam power is possible by upgrading the AGS repetition rate to 5 Hz and increasing the linac energy to 1.5 GeV, which allows for doubling the number of protons per pulse to 2×10^{14}. To achieve the required bunch length compression a separate compressor ring would be needed. This ring will

- operate below transition
- have a small slippage factor, that is, it will be quasi-isochronous
- have low dispersion
- have an acceptance to emittance ratio > 8 (to be compatible with the tight beam loss limit)
- have a chromaticity correction system

Table B.1 summarizes the key parameters of the compressor ring. As discussed in Section B.1.2, the performance penalty of operating with longer bunches is not severe, so the cost-benefit evaluation of the compressor ring must be considered carefully.

Table B.1: Compressor ring parameters.

Circumference (m)	200
Bending field (T)	4.15
Kinetic energy (GeV)	24
Transition gamma	38.4
η	0.00074
Betatron tune, x/y	14.8/9.2
Maximum beta function, x/y (m)	12.9/19.8
Dispersion function (m)	0.12
Chamber radius (mm)	25
Maximum beam radius, x/y (mm)	7.0/8.6
Acceptance, x/y (m)	48.5/31.6
Beam emittance, x/y (m)	3.8/3.8
Accep./emit. ratio, x/y	12.8/8.3
Natural chromaticity, x/y	$-2.5/-1.7$

In operation, an unmatched bunch is injected from the AGS into the compressor ring. It is extracted immediately after a bunch rotation (bunch rotation takes a quarter of a synchrotron period, *i.e.*, 3 ms, or 4500 turns). Because of the very small slippage, a low rf voltage is required (see Table B.2.)

Table B.2: rf parameters of compressor ring.

RF frequency (MHz)	5.94
Harmonic number	4
V_{rf} (kV)	200
Bucket height, in $\delta p/p$	0.042
Bucket area (eVs)	222
Bunch area (eVs)	10
f_s, center (Hz)	91.5
f_s, edge (Hz)	82.6

The longitudinal parameters of the ring are summarized in Table B.3

Clearly, the longitudinal microwave instability threshold will be low at the injection energy, because of the small slippage factor and the low $\delta p/p$. To reduce the impedance, the vacuum chamber will have smooth tapered transitions. However, we do not plan

Table B.3: Longitudinal parameters of compressor ring.

	Injection	Extraction
No. particles per bunch (10^{14})	0.17	0.17
RMS bunch length (m/ns)	5/17	0.9/3
Peak current (A)	65	363
Momentum spread (%)	0.4	2.24
Longitudinal emittance (eVs)	10.5	10.5
Broadband impedance ($j\Omega$)	5	5
Space-charge impedance ($j\Omega$)	1.66	1.66
Keil-Schnell threshold (jMΩ/m)	3.75	25.5
Effective rf voltage (kV)	200	248

to shield the bellows to avoid possible problems with arcing. Despite this we expect to achieve a broad impedance of 5 Ω, which is acceptable.

We see from Table B.3 that the combination of the broadband and the space-charge impedance is 3.34 Ω, slightly lower than the Keil-Schnell (KS) threshold. Since the beam is below transition, beam instability is not expected. The overall inductive impedance below transition has a focusing effect, which increases the effective rf voltage in the bunch rotation.

Table B.4: Transverse parameters.

	Injection	Extraction
Broadband impedance (jMΩ/m)	0.51	0.51
BB imp. induced tune shift	0.0003	0.0017
Space-charge induced tune spread	0.003	0.016
Chromatic tune spread	0.22	1.32
Chromatic frequency (GHz)	59.4	59.4

In Table B.4 we summarize the transverse parameters of the compressor ring. We find that the transverse impedance is low, as expected for a small ring ($Z_T \propto R$). Compared with the AGS, the compressor ring is transversely more stable (this is just opposite to the situation in case of longitudinal instability). The space-charge incoherent tune spread is small and is helped by the strong focusing optics. If the chromaticity were not corrected, the chromatic tune spread would be large. This is due to the small slippage factor, the high revolution frequency, and the high tune. For these reasons, we will control the normalized chromaticity to about 1%.

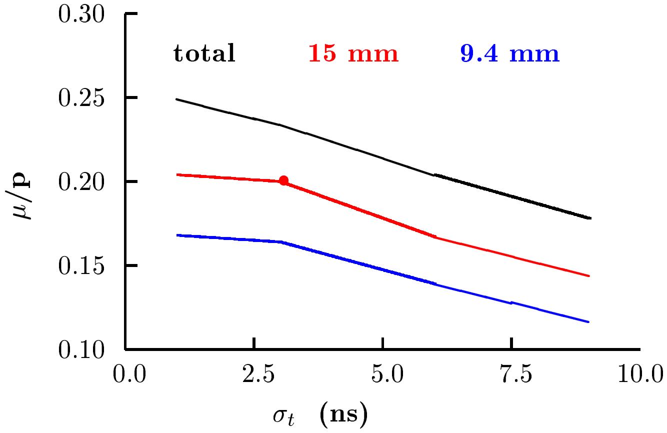

Figure B.1: Efficiency *vs.* proton bunch length.

The compressor ring design requires very low rf voltage; also, the potential-well effect facilitates the short bunch production. The required impedance is reasonable to achieve, and the acceptance/emittance ratio of 8 units is much larger than that for existing and proposed high intensity proton accelerators. In conjunction with the large momentum aperture it is reasonable to expect that beam losses can be controlled. Chromaticity control at the compressor ring is not easy, however, and needs further studies.

B.1.2 Proton Bunch Length and a Buncher Ring

The minimum proton driver bunch length achievable is set by the longitudinal emittance of the bunches and by the momentum acceptance of the AGS. For the baseline 1 MW case, we expect to achieve the specified rms bunch length of 3 ns without a bunch compressor ring.

However, if the proton bunch intensity is increased by a factor of two to reach 2 or 4 MW, as discussed in Section B.1, then the bunch length would be expected to increase,

Table B.5: Efficiency *vs.* proton bunch length.

rms bunch length (ns)	μ/p	relative
1	0.204	1.02
3	0.20	1.0
6	0.167	0.835
9	0.144	0.72

and the specified 3 ns rms bunch length could not be achieved without increasing the momentum spread above the AGS acceptance.

The consequence of such an increase in bunch length was simulated, without reoptimization. (It is not expected that any reoptimization will markedly improve the result.) The final muon per proton ratios obtained are given in Table B.5 and Fig. B.1. Note that the cooling system used in this early study had larger apertures, and thus higher performance, than the final design, but the sensitivity to bunch length is expected to be the same. It is seen that there is relatively little gain for pulse lengths less than 3 ns (the baseline value). For a 6 ns bunch the efficiency has dropped 16.5%, and for 9 ns, the efficiency has dropped by 28%.

B.2 Target

B.2.1 Rotating Inconel Band Option

If unforeseen difficulties make a liquid metal target undesirable, there are several alternatives. One of them, is a moving metal band target. The performance would be little different from the metal jet. The scheme is discussed in the next Section.

B.2.1.1 Introduction and Overview

As a backup scenario to the baseline mercury jet target design, we present here a solid-target option that is based upon an Inconel Alloy 718 target in a rotating band geometry. Similar conceptual designs for rotating band targets have been presented previously [1, 2, 3] for use at both muon colliders and neutrino factories. A more detailed report on this particular conceptual design can be found in reference [4].

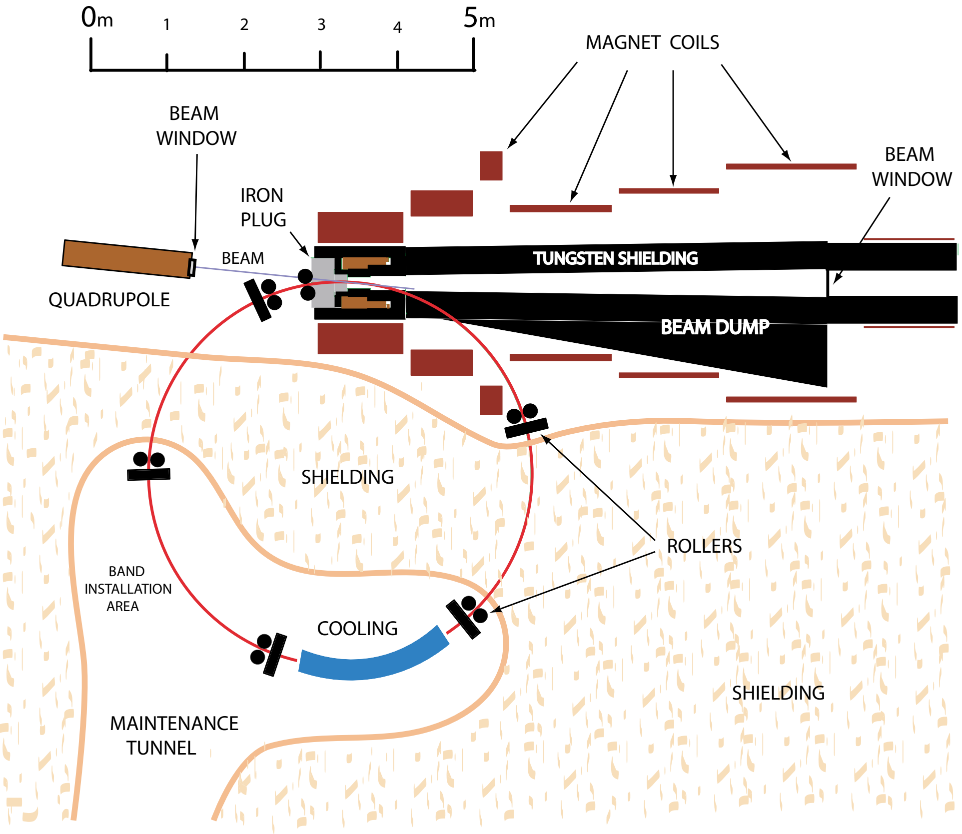

Figure B.2: A conceptual illustration of the setup for a pion production target based on a rotating inconel band.

A plan view of the targetry setup for the band target option is shown in Fig. B.2. An Inconel target band threads through the solenoidal magnetic capture channel to tangentially intercept the proton beam. The circulating band is cooled by passage through a water tank located in a radiation-shielded maintenance enclosure.

Inconel 718 is a niobium-modified nickel-chromium-iron superalloy that is widely used in nuclear reactors and particle accelerator applications because of its high strength, outstanding weldability, resistance to creep-rupture due to radiation damage and resistance to corrosion from air and water. The Inconel target band has an I-beam cross section. The band dimensions and positioning relative to the proton beam are shown in Fig. B.3. The proton pulse structure and bunch charges were assumed to be identical to the base-line target scenario. Table B.6 presents the parameter specifications that have been assumed

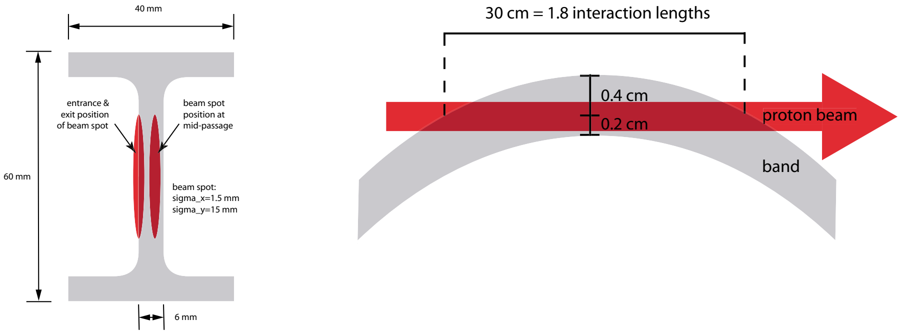

Figure B.3: Passage of the proton beam through the target band shown in cross-sectional (left) and plan (right) views. The horizontal position of the beam spot in the band webbing varies along the interaction region due to the curvature of the band. The plan view shown in the right plot is anamorphic, with a 10:1 aspect ratio.

for the Inconel target band and the incident proton beam.

B.2.1.2 Mechanical Design Considerations

As is evident from Fig. B.2, threading the target band through the pion capture channel requires only slight variations on the channel design assumed for the baseline mercury jet target option. An entry port must be incorporated into the iron plug in the upstream end of the capture solenoid and an exit port traverses the tungsten shielding and then passes between the solenoidal magnet coil blocks and out of the pion decay channel. The exit port can either be designed into the magnet cryostat or else the cryostat can be partitioned longitudinally into two cryostats so the band can exit between them. The radius of the third magnet coil block from the upstream end of the channel must be increased by approximately 10 cm relative to the baseline design in order to provide adequate space for the band to exit the channel. A modest reoptimization of the magnet coil currents in this region can restore the baseline magnetic field specifications.

No detailed consideration has yet been given to the design of the beam dump. As is clear from Fig. B.2, the target band exit port is far enough upstream from the beam dump for it to be essentially ddecopled from the beam dump design.

The band is guided and driven by several sets of rollers located around its circumference, as shown in Fig. B.2. A few hundred watts [4] of drive power will be required due to the eddy current forces from the band entering and exiting the 20 T solenoid.

Table B.6: Specifications of the Inconel target band and assumed proton beam parameters.

Target band radius, R (m)	2.5
Band thickness, t (mm)	6
Band webbing height, h (mm)	60
Full width of band flanges (mm)	40
Beam path length in band, L (cm)	30
Proton interaction lengths, λ	1.81
Density of Inconel 718, ρ (g.cm^{-3})	8.19
Mass of band (kg)	98.8
Band rotation velocity, v (m/s)	1
Proton energy (GeV)	24
Protons/bunch	1.7×10^{13}
Bunches/fill	6
Time between extracted bunches	20 ms
Repetition rate for fills	2.5 Hz
Horizontal beam-channel angle, α (mrad)	100
Beam spot size at target (horizontal), σ_x (mm)	1.5
Beam spot size at target (vertical), σ_y (mm)	15.0

Following the lead of the BNL g–2 target design [5], the roller assemblies will all incorporate self-lubricating graphalloy [6] bushings that are compatible with high radiation environments.

The pion production region of the target is in an air environment, with beam window positions shown in Fig. B.2. This simplifies target maintenance and target band replacement by avoiding any requirement to break and re-establish seals in a high radiation environment. Activated air and gases from the target and interaction region are continuously diluted and then vented from the target hall into the outside atmosphere following the procedure adopted [5] for the BNL g–2 target.

The heated portion of the band rotates through a 2-m-long cooling tank [4] whose conceptual design is shown in Fig. B.4. The band entrance and exit ports in the ends of the tank also serve as the water outlets. Both the heat transfer rates and water flow rates are found [4] to be relatively modest and the water flows due to its gravitational head alone with no need for forced flow.

The rotation of the target band has the desirable dilution effect that the rate of radiation damage on any particular section of the band material is reduced by roughly two

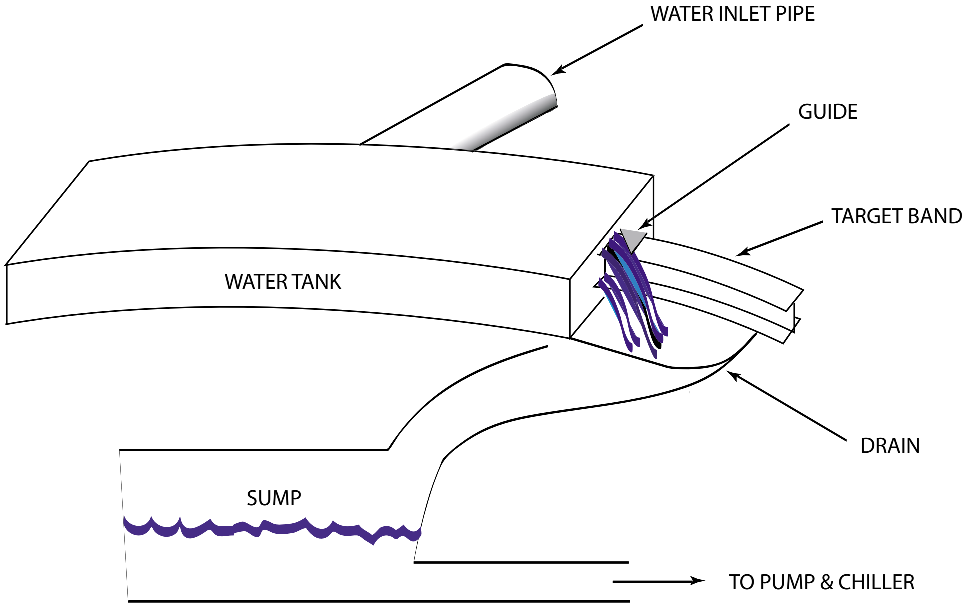

Figure B.4: A conceptual illustration of the cooling setup for the Inconel target band.

orders of magnitude relative to a fixed target geometry, since the 15.7-m-band circumference corresponds to 95 interaction lengths. Hence, each target band may last for several years [4] before requiring replacement.

The heavily irradiated used bands will be remotely extracted by progressively clamping and then shearing off 1 meter lengths and dropping them into a hot box. After the removal of the hot box, the band maintenance area can then be accessed and the new band progressively installed by welding together, in situ, eight 1.96-m-long chords of target band that have been previously cast (or otherwise prepared) into the correct I-beam cross section and circumferential curvature. Beam-induced stresses on the welds are minimized by welding on the flanges of the I-beam rather than on the central webbing; the flanges are not directly exposed to the proton beam and will also receive much smaller energy depositions from secondary particles than the central webbing.

B.2.1.3 Simulations of Pion Yields and Beam-Induced Stresses

Full MARS [7] tracking and showering Monte Carlo simulations were conducted [4] for 24 GeV protons incident on the target, giving predictions for the pion yield and energy deposition densities.

The yield per proton for pions plus kaons plus muons at 70 cm downstream from the central intersection of the beam with the target was predicted [4] to be 0.715 (positive) and 0.636 (negative) for the momentum range $0.05 < p < 0.80$ GeV/c, and 0.304 (positive) and 0.288 (negative) for the kinetic energy range $32 < E_{kin} < 232$ MeV that approximates the capture acceptance of the entire cooling channel. Note that the material in the flanges of the I-beam was not included in the calculation; their inclusion might result in a small change in the predicted yield. For comparison, the predicted yield was 18% higher for the identical geometry but with the band material artificially changed from Inconel to mercury.

Approximately 7% of the proton beam energy is deposited in the target as heat and the maximum instantaneous energy deposition from a single proton bunch is approximately 13 J/g, which corresponds to a temperature rise of approximately 29 °C. Detailed 3-dimensional maps of energy deposition densities were generated for input to dynamic target stress calculations [4] using the commercial ANSYS finite-element analysis code.

For the ANSYS simulations, the target band geometry was discretised into a 3-dimensional mesh containing approximately 30,000 elements. It was conservatively assumed that all of the deposited energy from a proton pulse is instantaneously converted into a local temperature rise.

The von Mises stress (*i.e.*, the deviation from the hydrostatic state of stress) was found to be initially zero but to develop and fluctuate over time as the directional stresses relax or are reflected from material boundaries. Figure B.5 gives a snap-shot of the predicted von Mises stress distribution at 1μs after the arrival of a proton pulse and Fig. B.6 shows the time development of the predicted stress at the position of maximum stress. For Fig. B.6, a “fixed edge” constraint has been applied to the band model with a simple rectangular cross section that is shown in the preceding figure; this is intended to better approximate the stiffening from the I-beam flanges in the actual band without the extra computing capacity required to simulate the more complicated true geometry. The predicted 190 MPa peak value, in both time and position, for the von Mises stress from a single proton bunch is much less than the the 740 MPa (or 1100 MPa) yield strength for annealed (or precipitation hardened) Inconel 718 and is also well below its fatigue strength.

The band rotation speed, 1 m/s, advances the band by 40 cm between successive beam fills. This presents a fresh 30 cm chord of target band for each beam fill, but the energy depositions from the 6 bunches within the fills are largely superimposed. However, the pile-up of stresses is not considered serious since any significant level of von Mises stress is expected to die out well within the 20 millisecond time span between successive

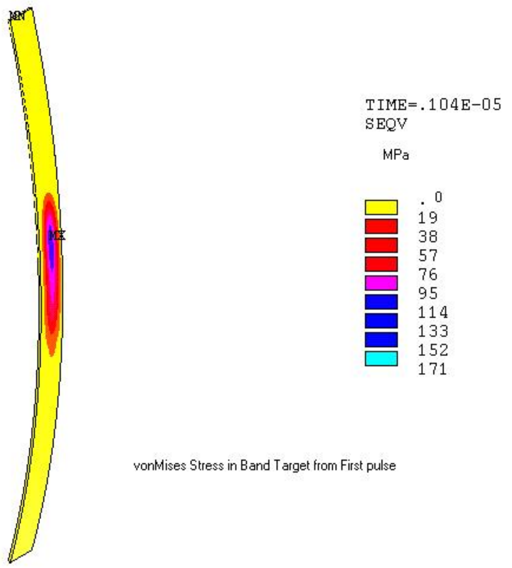

Figure B.5: Predicted von Mises stress distribution for the target band model at 1 μs after the arrival of the proton pulse. For simplicity, the flanges of the I-beam have been neglected in this particular simulation run. The maximum predicted von Mises stress at this time is 171 MPa.

bunches (*i.e.*, approximately 3000 times the time interval plotted in Fig. B.6), leaving only the relatively benign hydrostatic stresses.

B.2.1.4 Summary

In summary, the Inconel rotating band target design appears to be a promising backup option to the baseline mercury jet target. The pion yield appears slightly lower than the mercury baseline, although this has yet to be fully optimized. The engineering design looks manageable and initial simulations of target stresses are encouraging.

B.2.2 Carbon

As demonstrated in Study-I [8], a radiation cooled graphite target could be used up to 1.5 MW power level. It appears to be a relatively conservative solution (at 1 MW) but would sacrifice a factor of 2 in performance and require relatively frequent replacement. It is unclear if it could be used at 4 MW.

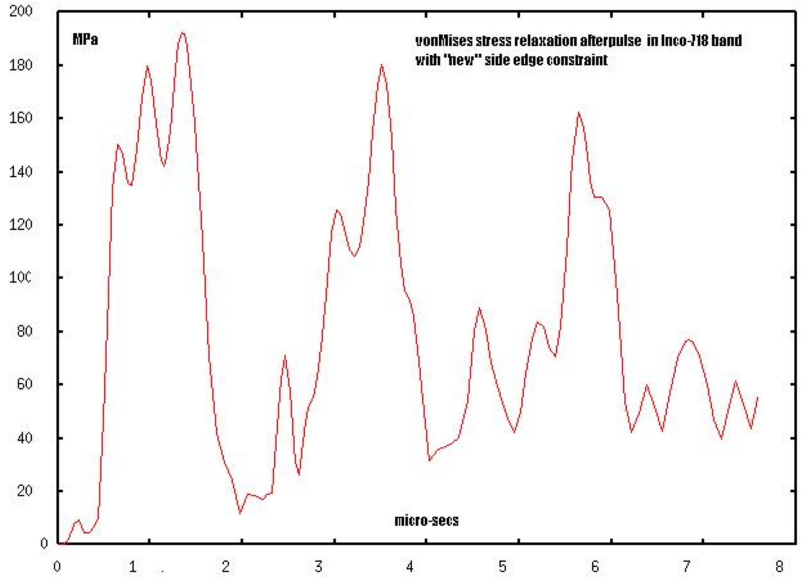

Figure B.6: Predicted time dependence of von Mises stresses on the target band. The time origin corresponds to the arrival of the proton pulse.

B.2.3 Granular

A "granular" target has also been suggested recently as an alternative approach, but this has not been examined during Study-II. [9].

B.3 Phase Rotation

B.3.1 Correlation Matching

Within the cooling lattice, particles with high transverse amplitude travel on longer orbits than those on the axis and thus, for a given momentum, move more slowly in the forward direction. In such a lattice, with active rf, the average forward velocity is controlled by the phase velocity of the rf and constrained to a fixed value. As a result, the stable momentum of a particle is dependent on its amplitude

$$\frac{dz}{dt} - \beta c \;\propto\; A^2, \tag{B.1}$$

where the approximately conserved particle amplitude is given by,

$$A \;=\; \frac{x^2+y^2}{\sqrt{\beta}} \;+\; \sqrt{\beta}\,(x'^2+y'^2). \tag{B.2}$$

Such a correlation is also generated naturally in the phase rotation process but, since the phase rotation is done in a different lattice from the cooling, the magnitude of the correlation is not the same. As a result, there is, in the present design, a mismatch in correlation at the entry to the cooling channel. Study is needed to see if performance could be improved by better matching to the optimal correlations, possibly by raising the solenoid fields used in the transport and phase rotation channels.

B.3.2 Polarization

A system of double phase rotation has been studied [10] that generated a strong correlation between the muon polarization and final time after the phase rotation. This correlation, though a little diluted, is maintained through to the storage ring and results in correlations between neutrino type and time of detection. The physics need for such correlation has not been well established, and the system requires high gradient (4 MV/m) low frequency (30 MHz) rf close (3–6 m) to the target. The viability of rf in such high-radiation environment has been questioned, but tests at CERN [11] suggest it may be feasible if it is needed.

B.3.3 Bunched Beam Phase Rotation

Cost savings may be possible by performing the phase rotation with rf after bunching of the beam [12]. As in induction linac phase rotation, the bunch is first allowed to drift to increase the bunch length and establish a correlation between time and energy, but in this case the bunching is done before the energy is corrected. The rf that performs this bunching is acting on a beam with strong time-momentum correlation; *i.e.* a beam whose time spread is still increasing with drift distance, and whose sub-bunches, as they are formed, have spacings that are also increasing. This requires that the rf wavelengths used to create and hold the bunches also rise with drift distance. After the bunches have been formed, suitable modifications to the rf frequencies and phases can be employed to accelerate the later bunches and decelerate the early ones, thus ending up with a train of bunches at a single energy, as in the conventional case.

The need to have cavities operating at many different frequencies is certainly a complication. But since the cost of conventional rf acceleration is likely to be less than that for induction acceleration, the cost of the system is expected to be less. Whether it is as efficient is less clear. For instance, non-distorting phase rotation does not seem possible with the rf-based scheme. But this scheme has the interesting feature of working on muons of both signs—the bunches of the opposite sign automatically form between the others. If both signs were subsequently accelerated through the linacs and RLA (injected in the opposite direction), and injected into the storage ring (also in the opposite direction), then a factor of two in efficiency could be achieved. This factor of two might compensate for any lower efficiency in the phase rotation of muons of one sign.

This solution is far from worked out, but seems worth evaluating. Injection into the ring must be such that timing can be used by the detector to separate the neutrinos from the two different muon trains.

B.4 Cooling

B.4.1 Limited-Flip Cooling Channels

In all solenoid focused channels used for cooling, the axial direction of the field must be reversed, at least once. If this is not done, canonical angular momentum (*i.e.*, the angular momentum of the beam once out of the axial field) rises, and it is impossible to remove it. In the SFOFO lattice, the field is reversed every cell, and significant canonical angular momentum never develops. But there are other solutions with far fewer flips: *e.g.*, single flip [13] or double flips, as in the example in Section B.4. In these cases the canonical angular momentum is allowed to build up, but is subsequently removed after a flip by cooling with the opposite field direction. The performance of such alternatives appears to be similar to that of the SFOFO, but the engineering design of the magnets is very different. The SFOFO has about five times less stored magnetic energy (often considered an indicator of cost) than the double flip design, but the forces between the coils are higher. At this time, the Super FOFO seems more cost effective, but more detailed engineering will be needed to confirm this.

There is another difference between the baseline design and the double-flip alternative (see Section B.4), that is unrelated to their differing lattices. The double-flip alternative performs its cooling at higher energy, and along the lattice. This gives a larger longitudinal acceptance, but requires more rf acceleration for a given cooling. The larger acceptance preserves more muons through the cooling channel, but does not appear to increase the muons accepted by the current acceleration scheme (see Section 6). Further optimization will be needed to assess the possible benefits of this alternative cooling channel design.

B.4.2 The Double-Flip Cooling Channel

B.4.2.1 Introduction

Unlike the baseline SFOFO channel, the Double-Flip (DF) channel [15] is based on long solenoids. Cooling is performed in a constant, or adiabatically increasing, magnetic field. This configuration provides simple transverse optics: for a matched beam there is neither modulation of the beam envelope along the channel, nor large chromatic effects.

A uniform solenoid that contains absorbers and rf cavities can only cool in two of the four transverse degrees of freedom: the Larmor radii of all the particles decrease while the positions of their Larmor centers remain unchanged. For an infinitely long channel, if we neglect scattering, the muon helices would therefore shrink to lines, and the resulting beam would be wide but without any angular spread. The magnetic field must be reversed at least once to achieve cooling in four dimensions (p_x, p_y, as well as x and y).

The field-flip section should be as short as possible (fast field flip) to avoid mismatching the beam in the region of zero field. At the flip region, the Larmor centers would move from one vertex of a parallelogram in x–y space to the opposite one, as shown in Fig. B.7 (Larmor radius $\Longleftrightarrow$ Larmor center exchange). The lengths of the channel sections with positive and negative magnetic field can be chosen to achieve a “canonical” phase ellipse on exit (an ellipse with zero angular momentum and no x–p_x correlations).

The major disadvantage of a cooling channel based on long solenoids is the perturbation of the longitudinal motion at the field flip regions. The longitudinal velocity is expressed as:

$$V_z = \frac{c}{E}\sqrt{E^2 - m^2c^4 - p_T^2c^2}\,, \tag{B.3}$$

where E and p_T are the total energy and transverse momentum of the particle. Due to the presence of an accelerating field, V_z oscillates around an equilibrium value equal to the phase velocity of the accelerating wave V_{ph}. It is possible to find the equilibrium energy that satisfies $V_z(E_{eq}) = E_{ph}$:

$$E_{eq} = E_{nominal}\sqrt{1 + p_T^2/(mc)^2}\,, \tag{B.4}$$

where $E_{nominal}$ is the usual nominal energy:

$$E_{nominal} = \frac{mc^2}{\sqrt{1 - V_{ph}^2/c^2}}\,. \tag{B.5}$$

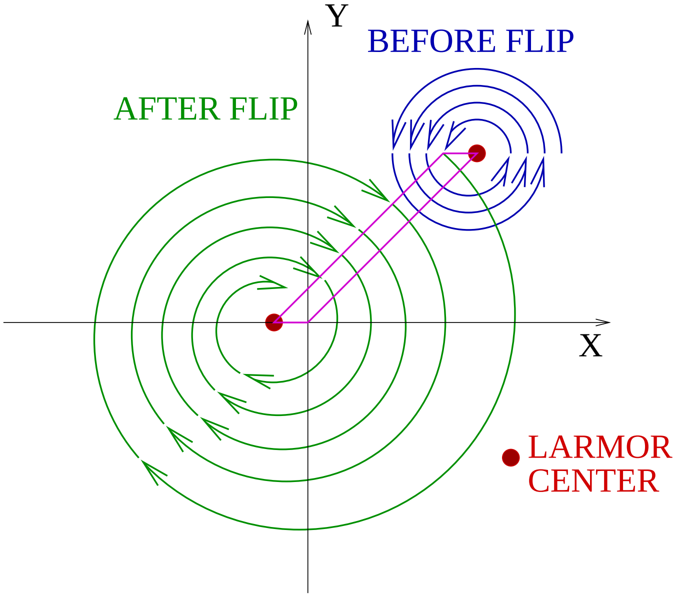

Figure B.7: Illustration of the particle motion before and after the first flip region (end view).

E_{eq}, as well as the separatrix, depends on transverse momentum and changes at the field flip. Typically, p_T is small immediately before the field reversal due to the cooling achieved in the section that precedes the flip. But after the field flip:

$$p_T \simeq \frac{eBr}{c} \tag{B.6}$$

where r is the particle radius.

The corresponding jump in the equilibrium energy leads to a strong perturbation of the synchrotron oscillations. This effect is mitigated by using a small magnetic field before and immediately after the first flip region. The field then grows adiabatically to decrease the β-function and maximize the cooling. The beam, however, would have a non-zero angular momentum its exit from such a system. A second field-flip section in the high field region, followed by a short additional cooling section, is therefore necessary to suppress the residual angular momentum. Due to the small beam radius at the end of the third section, the perturbation to the longitudinal motion at the second field flip is small. From these considerations, the DF channel is designed as follows (see Fig.B.8): the first section cools the transverse momenta of the muons using a relatively low constant solenoidal field (3 T on axis). Because the magnetic field is constant, the Larmor centers of the particle motion are unchanged and the transverse size is constant to first order. In the short region between sections 1 and 2, following the field reversal, the centers of the Larmor orbits are displaced and in section 2 the muons, to first order, execute Larmor motion about the solenoid axis. Then, the field is increased adiabatically up to -7 T in order to focus the beam more strongly, reducing the β-function for cooling of both the beam size and the transverse momentum. The second field flip is, therefore, performed at -7 T. The section lengths are chosen to obtain a canonical beam without parasitic correlations at the end of the channel. The beam is slowly accelerated to compensate for longitudinal emittance growth and avoid particle losses. The full length of the cooling channel is approximately 217 m.

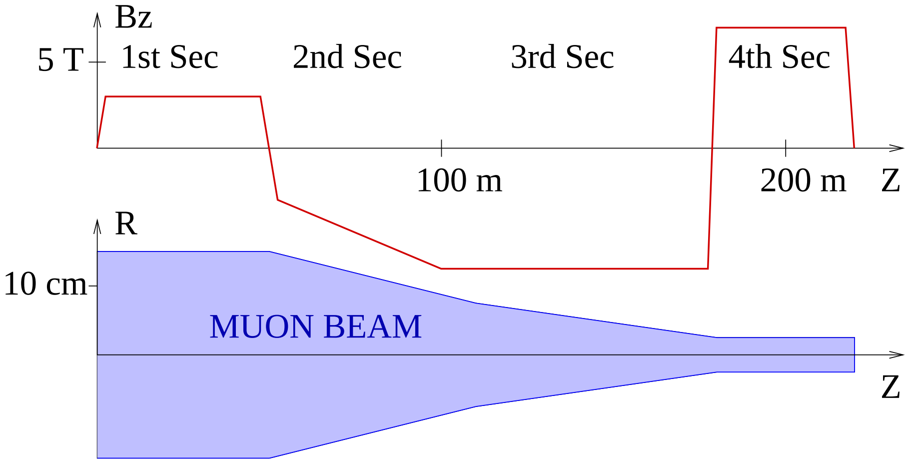

Figure B.8: Sketch of B_z on axis and the beam envelope associated with the double-flip channel.

B.4.2.2 Initial Constraints and the Input Beam

The optimization of any cooling channel is strongly coupled to the front-end design. The double-flip channel is optimized to maximize the transmission and the cooling performance for the input beam produced at the end of the pre-cooling system. The pre-cooling apparatus, and consequently the input beam for the double-flip channel, is different from the baseline system described in Chapter 5. It follows the design developed during Feasibility Study- ([16]), which is displayed in Fig. B.9. It consists of:

- **A: GeV proton beam**

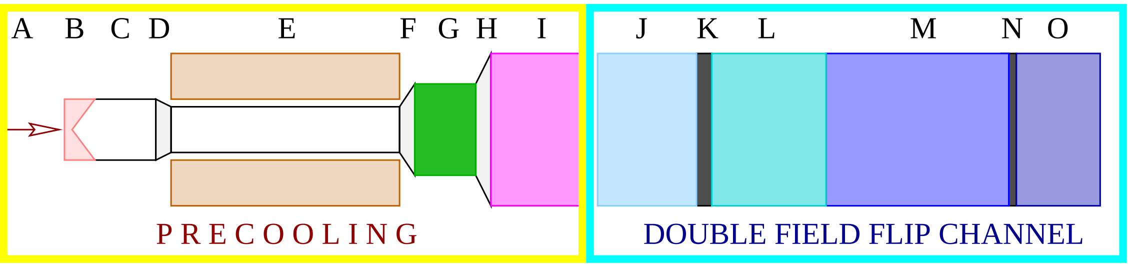

Figure B.9: Sketch of the accelerator system preceding the cooling channel (front-end).

The beam size is $\sigma_x = \sigma_y = 2.14$ mm, σ_t=3 ns.

- **B: Target station**
  A solid carbon target of 0.8-m length and 7.5-mm radius is placed in a 20-T solenoid. Then, the solenoidal field decreases adiabatically to 1.25 T in a 9 m long matching section.

- **C: Decay channel**
  A uniform solenoid, 41-m-long, with a radius of 30 cm and a field of 1.25 T on axis, is used.

- **D: 4-m-long matching section**
  The magnetic field increases from 1.25 T to 3 T, and the solenoid radius decreases from 30 cm to 20 cm, to provide a matching between the decay channel and the induction linac.

- **E: 100-m-long induction linac**
  It develops a voltage from −50 MV to 150 MV in a pulse. The accelerating voltage in the gaps is adjusted to accept muons in the energy interval 230 MeV $< E_{tot} <$ 330 MeV.

- **F: Matching section**
  A 0.6-m-long solenoid channel is used.

- **G: Minicooler**
  Minicooling is accomplished by a 2.6-m-long liquid-hydrogen (LH_2) absorber inside a 3 T solenoid with a radius of 40 cm. It produces some transverse cooling and decreases the average beam energy from 280 MeV to 200 MeV, which is optimal for bunching.

- **H: Matching section**
  A 0.3-m-long solenoid channel is used.

- **I: Buncher**
  It includes three accelerating stations and three drift spaces inside a solenoid with $r = 71$ cm, B= 3 T. Each station comprises six $f = 201$ MHz $\pi/2$ cavities, 32 cm long. The full voltages of the three stations are 15, 19.5 and 24 MV, respectively. The synchronous phase is zero at the total nominal energy of 200 MeV.

The performance of the cooling channel was tested using the beam coming from the end of the buncher (see Table B.7), as produced from a simulation of the precooling section [15]. Note that the product $\sigma_x \sigma_{p_x}/mc$ is greater than the beam transverse emittance ε_x due to the x–p_y correlations. Figure B.10 shows the distribution of particles in longitudinal phase space (energy *vs.* ct) for the "realistic" beam at the beginning of the cooling channel. Particles outside the separatrix will be lost ($\simeq$30%).

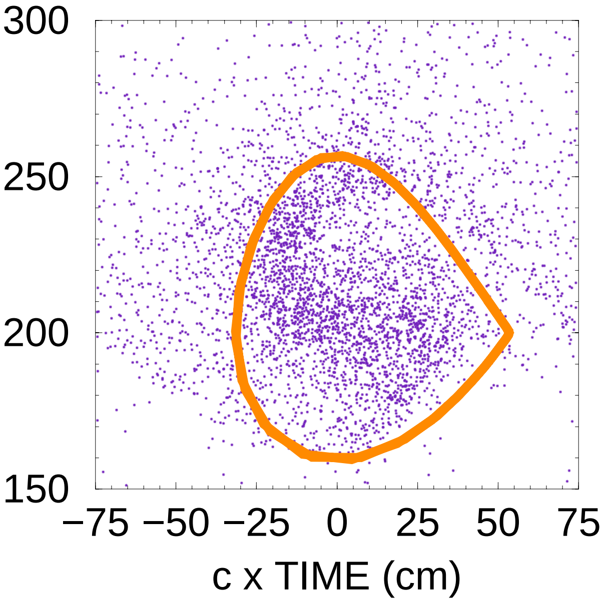

Figure B.10: Distribution of particles in longitudinal phase space for the "realistic" beam at the beginning of the cooling channel. Particles outside the rf bucket separatrix will be lost ($\simeq$30%).

The channel performance was also tested using a Gaussian beam with transverse parameters similar to those of the "realistic" beam and $\sigma_{ct} = 10$ cm, $\langle E \rangle = 200$ MeV, σ_E

= 20 MeV.

Table B.7: Parameters of the "realistic" beam (b) after bunching (input to the cooling channel), as calculated in Ref. [15]. "In bucket" means that the μ/p yield is calculated with respect to the particles inside the initial phase space bucket.

σ_x (mm)	σ_{p_x} (MeV/c)	$\sigma_x\sigma_x/mc$ (mm)	ε_x (mm)	μ/p E < 300 MeV	μ/p (in bucket)
54.6	24.4	12.6	11.1	0.191	0.135

In the "realistic" and Gaussian beam simulations, we use μ^+ particles, which describe a clockwise helix in a field $\vec{B_z} = B_z\hat{z}$.

B.4.2.3 Description of the Channel

The cooling lattice, simulated with GEANT4 [17], comprises four sections: the first contains 20 cooling cells, 2.42-m-long, in an almost-constant magnetic field of $B_z = 3$ T on axis. Between the first and the second sections there is a 1.02 m long matching section in which the field changes polarity. The second section consists of 20 cells, 2.42-m-long, with a field on axis which adiabatically (and linearly) grows from $B_z = -3$ T to -7 T on axis. It is followed by a third section, containing 32 cells, 2.51-m-long (the first two cells are still 2.42-m-long), with a field of $B_z = -7$ T on axis. The second field flip region is 1.26-m-long and is followed by the fourth section with 15 cells, 2.51-m-long, with a field of $B_z = 7$ T on axis. A cooling cell includes 6 rf cavities that provide an effective voltage of 15 MeV/m, and a vessel containing the liquid-hydrogen absorber material (LH$_2$). Gaps in the long solenoids are required for flexible rf power feeds and cooling devices to reach the rf cavities and absorber. Fig B.11 shows an engineering drawing of two cooling cells of the DF channel (note that there is just one 20-cm gap every $\simeq$5 m). Correction coils could be needed to bring the magnetic field back to a uniform value in the gap regions, and avoid a degradation in the channel performance. The current simulation models neither the gaps nor the associated correction coils.

Detailed specifications of the cooling sections and the two flip regions are given in Tables B.8 and B.9. Figure B.12 shows a side view (in wire-frame mode) of a cooling cell, including the solenoid, the linac, and the absorber.

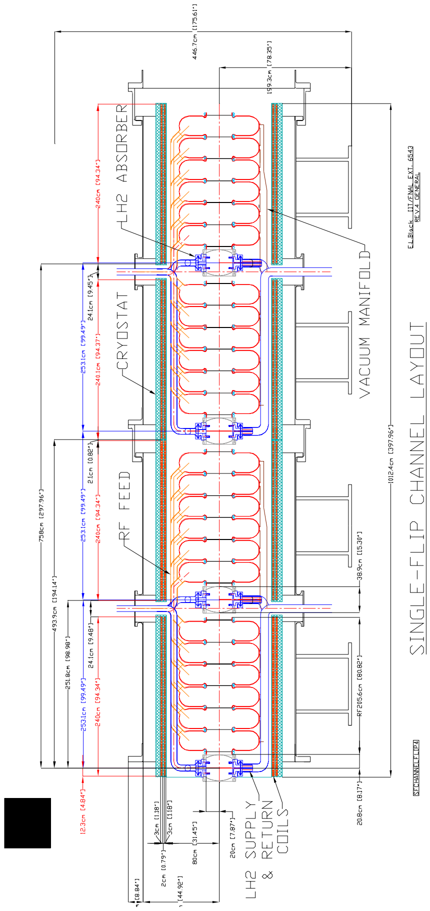

Figure B.11: Engineering drawing of a cooling channel unit cell. The gaps are not modeled in the simulation yet.

Table B.8: Lists of parameters associated with the four sections of the double flip channel.

Parameter	First	Second	Third	Fourth
Global	–	–	–	–
Length of section (m)	2.42	2.42	2.51	2.51
Magnetic field on axis (T)	3	$-3 \to -7$	-7	7
Mean current densities (A/mm^2)	68.2	$-22.7 \to -53.1$	-53.1	53.1
Coil thickness (cm)	3.5	10.5	10.5	10.5
Coil inner radius (cm)	81	81	81	81
Number of cells	20	20	32	15
Absorber	–	–	–	–
Length of hydrogen (LH$_2$) absorber (cm)	30	30	39	39
Density of LH$_2$ (g/cm^2)	0.0708	0.0708	0.0708	0.0708
Aluminum window thickness (μm)	360	360	220	220
Energy loss per cell (MeV)	10.4	11.2	$\approx$11.1	11.2
Radial aperture, in LH2 (cm)	16	16	7	7
Cavity	-	-	-	-
Length of rf cavity (m)	1.92	1.92	1.92	1.92
Number of rf cells per cavity	6	6	6	6
Frequency (MHz)	201.25	201.25	201.25	201.25
Effective voltage (MV/m)	15	15	15	15
Synchronous phase	25.5°	25.9°	24.6°	25.0°
Beryllium window thickness (μm)	300	300	25	25
Radial rf cavity aperture (cm)	16	16	7	7

B.4.2.4 Magnet

The coil blocks are modeled in the simulation as a set of infinitely thin current sheets separated 5 mm from each other in the radial direction. Each sheet shares an equal fraction of the total coil current. Figure B.13 shows the actual field, B_z on axis, as produced by the current distributions in the simulation.

The long solenoids are 81 cm in radius, and are designed so that they completely enclose the rf cavities. Coil thicknesses vary from 3.5 cm in the first section to 10.5 cm in the succeeding sections, as the magnetic field increases. The current densities of the thin and thick coils are 68.2 and 53.1 A/mm^2, respectively. The most sensitive parameter of

Table B.9: Parameters associated with the two flip regions of the double-flip channel. The main solenoid in the second flip region is made of three layers of conductor material with different current densities.

Parameter	Flip 1	Flip 2
Main Solenoid	–	(three layers)
Length (cm)	41+41	53.1+53.1
Gap length (cm)	20	20
Magnetic field at the coil (T)	3.15	6
Current density (A/mm^2)	68.2	38.6, 52.2, 68.2
Coil thickness (cm)	3.5	3.5, 3.5, 3.5
Coil inner radius (cm)	81	81, 84.5, 88
Inner solenoid	-	-
Length (cm)	10.5+10.5	24.5+24.5
Gap length (cm)	26.8	9.6
Magnetic field at the coil (T)	4.55	5.8
Current density (A/mm^2)	52.2	38.6
Coil thickness (cm)	24.42	15
Coil inner radius (cm)	21	11

the cooling channel is the gradient of the magnetic field in the field-flip regions. This gradient must be maximized in order to stabilize the longitudinal motion. Specifications for the two matching sections are displayed in Table B.9 and Figs. B.14, B.15. The 1.02-m-long first flip region consists of two outer coils, separated by 20 cm, and two 10.5-cm-long inner coils, separated by 26.8 cm from each other. The 1.26-m-long second flip region consists of the two outer coils, separated by 20 cm, and two 24.5-cm-long inner coils, separated by 9.6 cm. The magnetic fields on axis, B_z, associated with the matching sections are shown in Figs. B.16, B.17. Both sections achieve a field flip within a distance of less than 1 m.

The design of the solenoidal magnets is based on aluminum-stabilized superconductors with indirect cooling. This technique was initially developed for magnets used in particle physics detectors, which operate continuously for long periods of time in steady state conditions. Cooling of the magnets is accomplished by helium cooling tubes glued on the external face of the solenoids. In order to ensure the stability of the conductor, a minimum stability margin of 1°K is kept on the conductors. The operating point of the

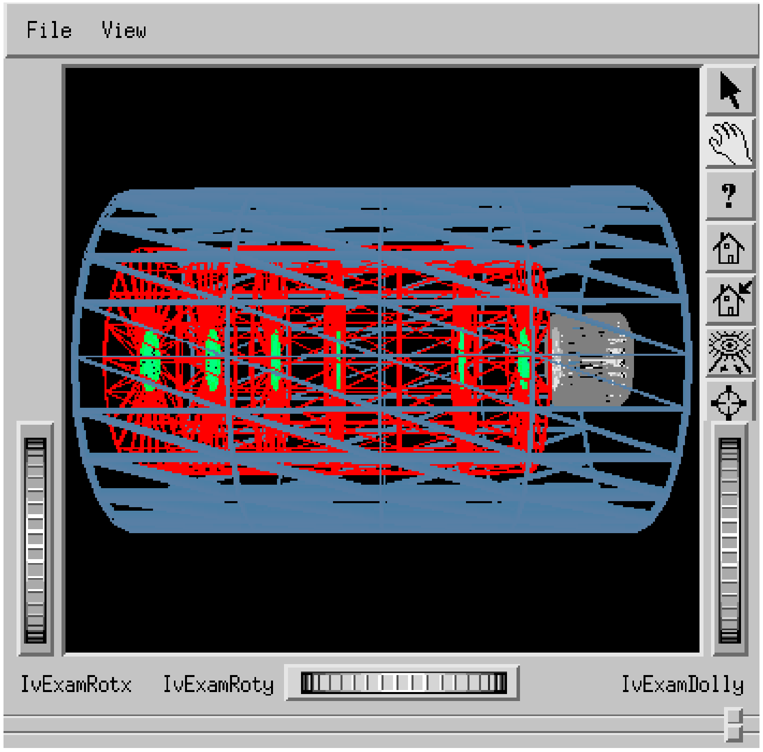

Figure B.12: Side view of a cooling cell as simulated in GEANT4 and visualized using the Open Inventor package [18].

conductor never exceeds 55% of its critical current at the operating field. The energy during a quench is dissipated inside the cold mass of the magnet. The magnets are quench protected, and the current induced in the mechanical structure during a fast discharge contributes to the propagation of the quench, thus limiting the temperature rise. The operating current is high, around 20 kA, in order to reduce the number of turns per magnet, and therefore limit their inductance. This reduces the time needed to discharge the magnets and limits the temperature rise during a quench. The aluminum stabilized conductors consist of NbTi superconducting cables around which an aluminum stabilizer is coextruded. The aluminum provides good mechanical and thermal stability, and ensures easy and safe processing during the winding (the superconducting cable is protected by the aluminum). The junction between conductors is done by TIG welding of the aluminum stabilizer. Since the critical current is strongly dependent on the magnetic field (in NbTi superconductor the critical current density decreases from 4500 A/mm^2 at 3 T to 1750 A/mm^2 at 7 T), it is advisable to use graded conductors for the cooling

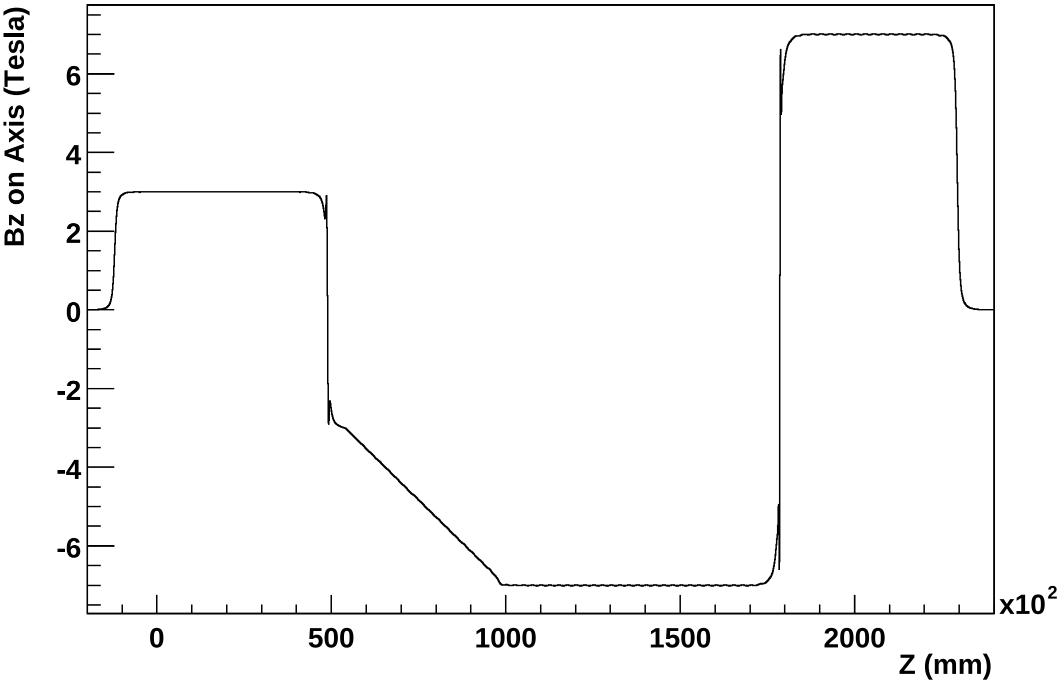

Figure B.13: B_z on axis as a function of z.

channel. In other words, the quantity of superconducting materials should be adjusted according to the location of the conductor in the magnet, leading to substantial savings in superconducting materials. As an example, a magnet operating at 20 kA, a cable having 32 strands of 1.4 mm in diameter, and a copper to superconductor ratio of 1.1 must be used in the innermost conductor layer. A cable having only 12 of the same strands is sufficient for the outermost layer. These design considerations lead to simple and safe magnets that can be easily built in industry and provide good reliability for long term operation under constant magnetic fields.

B.4.2.5 RF System

The rf system consists of one linac per cooling cell, each composed of 6 pillbox copper cavities, 32 cm long (phase advance is $\pi/2$). The radial aperture is 16 cm in the first two sections of the cooling channel and 7 cm in the third and fourth. Windows are made of Beryllium with thicknesses of 300 μm and 25 μm respectively. In the first two sections

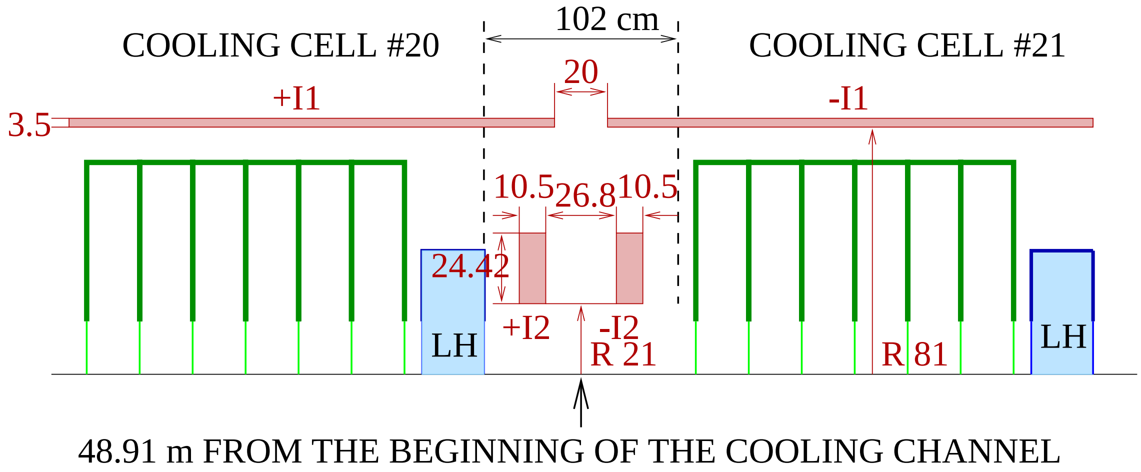

Figure B.14: The first matching section. The current densities I1 and I2 are listed in Table B.9.

the window thickness follows a step function which goes from 300μm to 600μm at 0.7 the full radius of the window. Figure B.18 shows a single r.f. cavity including the stepped window. Thin windows are preferred to reduce the transverse emittance growth due to multiple scattering. Mechanical constraints set a 25 μm lower limit to the thickness of a Beryllium window. The thickness must grow approximately as the fourth power of the radius to control the window temperature, which would rise due to the power dissipated by the high frequency electromagnetic fields. The optimal solution for the DF channel would be to adjust the window radius and thickness in each cell as the beam size decreases after the first flip. For simplicity, we changed the window size only once at the end of the second section.

A peak voltage of 16.48 MV/m, which corresponds to an effective voltage of about 15 MV/m, gives a large enough bucket to capture most of the beam from the buncher. The beam must be slowly accelerated to enlarge the bucket and compensate for the increase of the energy spread through the channel. This avoids particle losses due to longitudinal phase-space dilution. A particle with an energy of 200 MeV would lose about 10.4 MeV per cell in the first section and gain $\approx$12.9 MeV per 6-cell linac at a synchronous phase $\phi \approx 25.5°$. Fig B.19 shows the evolution of the nominal energy along the channel. It increases linearly from 200 MeV to 250 MeV in the first section. At the flip regions, the beam gains transverse momentum and its average longitudinal velocity decreases. The synchronous phases of the r.f. cavities are tuned taking into account a decrease of 15 MeV in the nominal energy of the channel at the flip regions. In the second section, the average

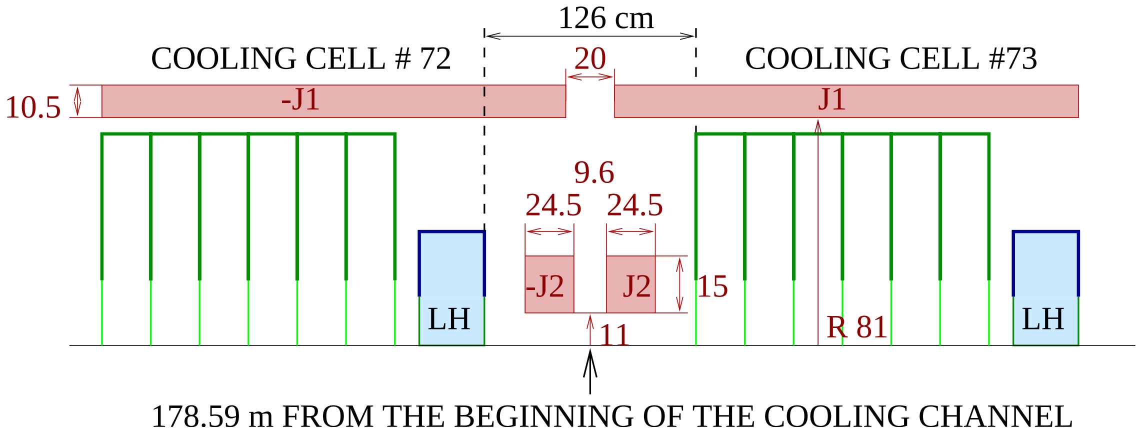

Figure B.15: The second matching section. The current densities J1 and J2 are listed in Table B.9.

net acceleration provided to the beam is the same as in the first, 2.5 MeV/cell. In the third and fourth sections, the acceleration is reduced to ≈0.85 MeV/cell. The nominal energy at the end of the fourth section is 326 MeV.

B.4.2.6 LH_2 Absorbers

The absorbers provide the energy loss necessary for the cooling mechanism. The hydrogen is contained by a cryostat vessel. The absorber length is 30 cm in the first two sections and 39 cm in the third (after the second cell) and fourth sections. This change compensates for the smaller dE/dx in the material as the energy increases, and approximately maintains the same synchronous phase throughout the channel. The aluminum windows have the same radius as the beryllium windows in the linac, but they must be thick enough to withstand the 1.2 atm pressure from the LH2. The windows are therefore 360 μm and 220 μm thick for a radius of 16 cm and 7 cm respectively. Fig. B.20 shows a downstream view of a unit cell with the absorber vessel (in grey) inside the solenoidal coils (in blue).

B.4.2.7 Performance

The performance of the channel described in the previous section, was studied using GEANT4 for both a Gaussian (a) and a “realistic” beam (b). For comparison, a third study (c) was done using a “realistic” beam through a modified version of the channel which follows more closely the design in Ref. [15]. In (c), only the windows are different: a radius and thickness of 20 cm and 125 μm for the aluminum windows in the LH2 vessels,

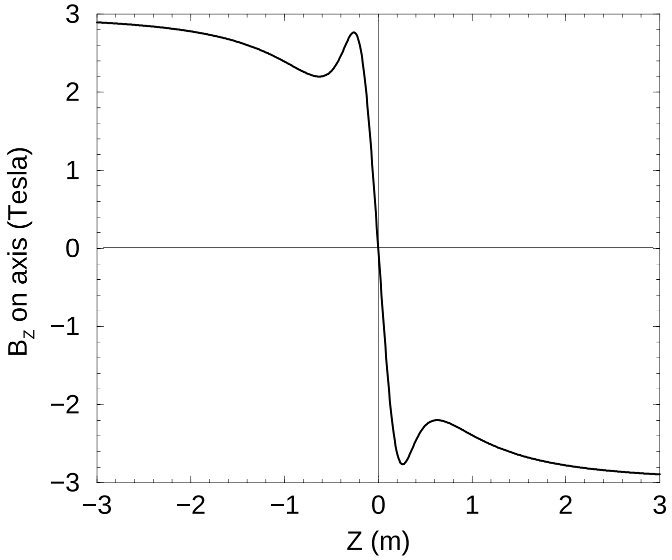

Figure B.16: The magnetic field on axis, B_z, around the first field-flip region. The z origin is placed at the center of the flip in this illustration.

and a radius and thickness of 20 cm (10 cm) and 400 μm (200 μm) for the beryllium windows in the r.f. cavities. In the three cases, muon decay is modeled and yields an $\simeq$8 % decrease in transmission. Table B.10 displays the beam parameters at the end of the cooling channel for (a), (b), (c), and Ref. [15].

Figure B.21, based on a 1000 particles simulation, illustrates the performance of the channel for the Gaussian beam (a). The transverse cooling factor is 6.5, from ε_x =12.6 cm to 1.92 cm. It is clear from Fig. B.21 that the first section of the DF channel reduces σ_{p_x} by a factor of two without changing the size of the beam envelope. The change of field polarity in the matching section causes σ_{p_x} to grow by a factor of 3. Due to the displacement of the Larmor orbits, the second section cools both σ_x and σ_{p_x}, to final values of 14 mm and 21.4 MeV/c, respectively. The second, third, and fourth sections recover from the transverse emittance growth in the field-flip regions, cool the transverse size of the beam, and restores angular momentum such that the beam is “canonical” when it exits the channel. The fractional transmission through this channel is approximately 69%.

Figure B.22, based on a 1000 particles simulation, illustrates the performance of the DF channel for the “realistic” beam (b). The final transverse and longitudinal emittances

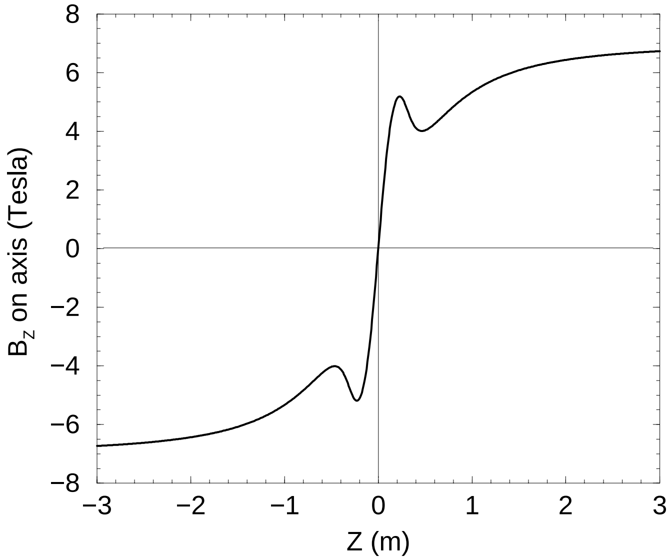

Figure B.17: The magnetic field on axis, B_z, at the second field-flip region. The z origin is placed at the center of the flip in this illustration.

(ε_x and ε_z) are 1.85 mm and 78 mm, respectively. The longitudinal emittance increases by a factor of 1.6 between the end of the first section and the end of the channel. Both σ_x and σ_{p_x} are cooled from initial values of 57 mm and 25.5 MeV/c to final values of 14.2 mm and 22 MeV/c, respectively. The transmission predicted by the GEANT4 simulation, referred to the total number of particles in the initial beam (with a E<300 MeV cut), is 40%.

Figures B.23, B.24, B.25 show the beam evolution as a function of distance from the origin. Plots number 0 and 19 correspond to the initial and cooled beam (before exiting the channel), respectively. Plots 4, 5, and 6 (13, 14, 15) show the beam immediately before, in the middle, and after the first flip (second flip) region. The rest of the plots are snapshots of the beam taken approximately every five cooling cells. The longitudinal phase space evolution in Fig. B.23 suggests that the bunch fills the 201.25 MHz r.f. bucket from the start. About half of the lost particles are muons that are not captured into the bucket; these are lost in the first few meters of the cooling channel. The remaining particle loss is due to the excitation of longitudinal motion in the first field-flip region. Low-momentum muons are lost at the maximum of the synchrotron oscillation, which is a few meters after the matching section. Thus the second section of the channel scrapes

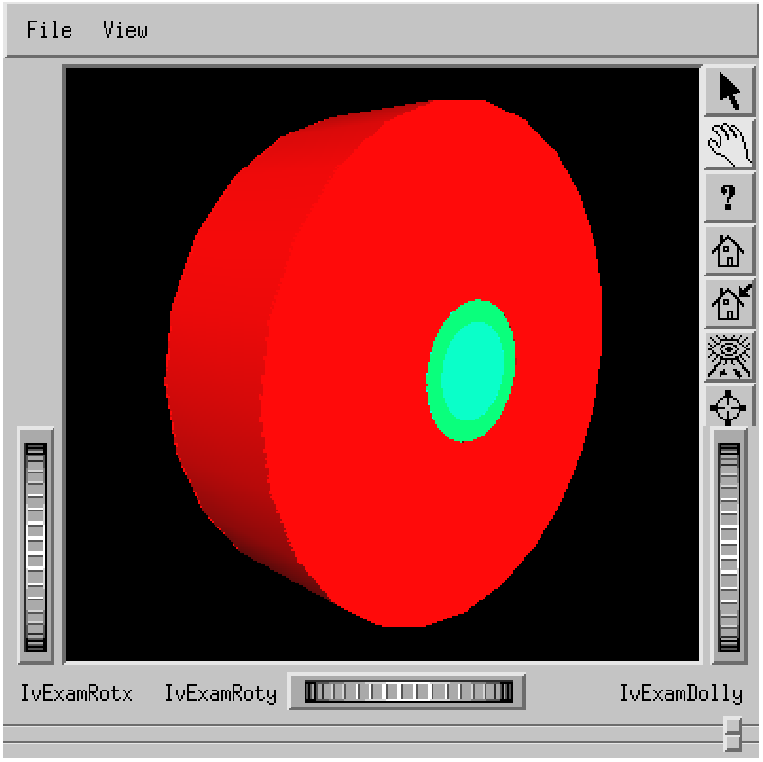

Figure B.18: Illustration of a single copper $\pi/2$ r.f. cell, 32 cm long, as simulated in GEANT4. The iris is covered by beryllium stepped windows: 300μm thick (r $< 0.7 \times$ R$_{\text{window}}$), 600μm thick ($r \geq 0.7\times$ R$_{\text{window}}$).

longitudinally. Figure B.24 illustrates on the transverse size of the beam, and Fig. B.25 on the angular momentum. Initially, the beam has a negative x - p_y correlation which is reversed in both field flip regions. On exit, the radial component of the fringe field would add the necessary contribution to suppress the beam angular momentum.

A "realistic" beam with non-optimized window dimensions (c) was used for comparison with results from the simpler simulation in Ref. [15]. The parameters at the end of the channel for (c) (or Ref. [15]) are in reasonable agreement: σ_x=14.4 mm (14.5 mm), σ_{p_x}=21 mm (21.1 mm), ε_x=1.74 mm (2.12 mm), ε_z=77 mm (74.6 mm). Transmission is 43% and 48% for (c) and Ref. [15], respectively.

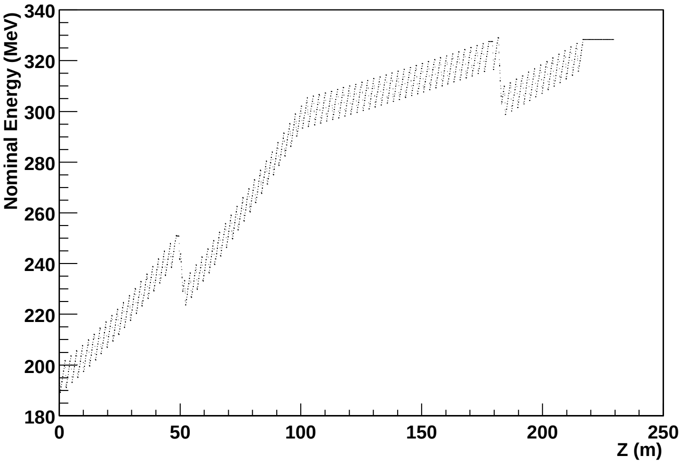

Figure B.19: Nominal energy of the channel *vs.* z. The nominal energy increases from 200 MeV to 326 MeV from the beginning to the end of the channel.

Table B.10: Parameters of the beam at the end of the cooling channel. $\star$ The longitudinal cooling factor is calculated with respect to ε_z at the end of the first section.

Case	σ_x (mm)	σ_{p_x} (MeV/c)	ε_x (mm)	Cooling factor (x)	ε_z (mm)	Cooling factor (z)	Transmission %
(a)	14.0	21.4	1.92	6.5	61.5	$0.43^\star$	69
(b)	14.2	22.0	1.85	6.8	77.6	$0.62^\star$	40
(c)	13.8	21.0	1.74	7.2	73.6	$0.69^\star$	43
Ref. [15]	14.5	21.1	2.12	6.0	74.6	$0.69^\star$	48

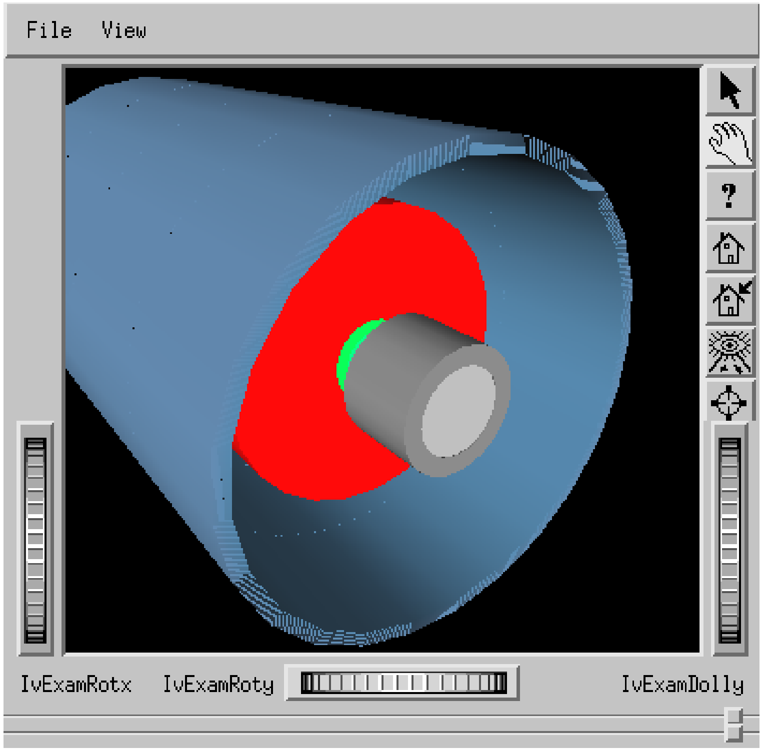

Figure B.20: The absorber vessel (in grey) is placed inside the solenoidal coils (in blue) in a unit cell. The aluminum windows are shown in light grey.

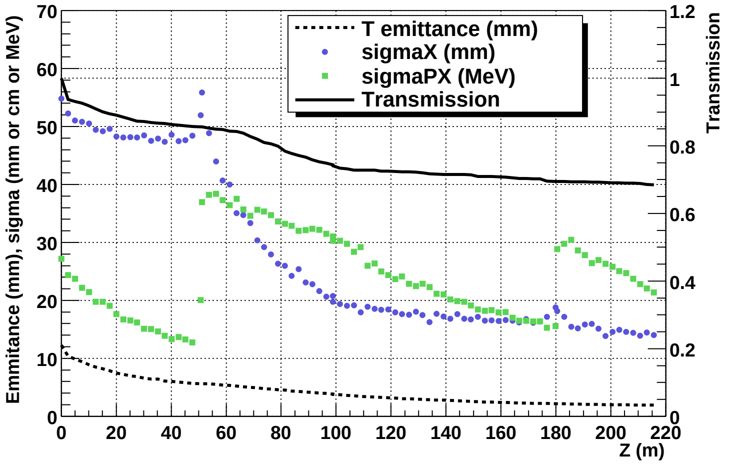

Figure B.21: Performance of the Double-Flip cooling channel with a Gaussian initial beam ("case a").

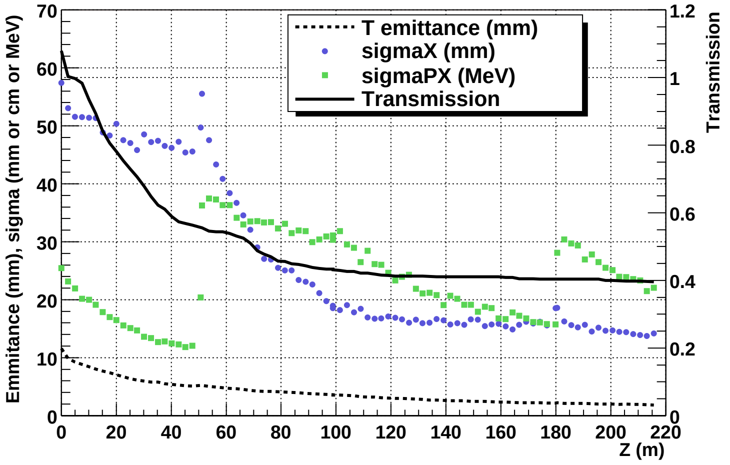

Figure B.22: Performance of the Double-Flip cooling channel with a "realistic" initial beam ("case b"), where the beam was generated from particle production at a carbon target and transported to the cooling channel.

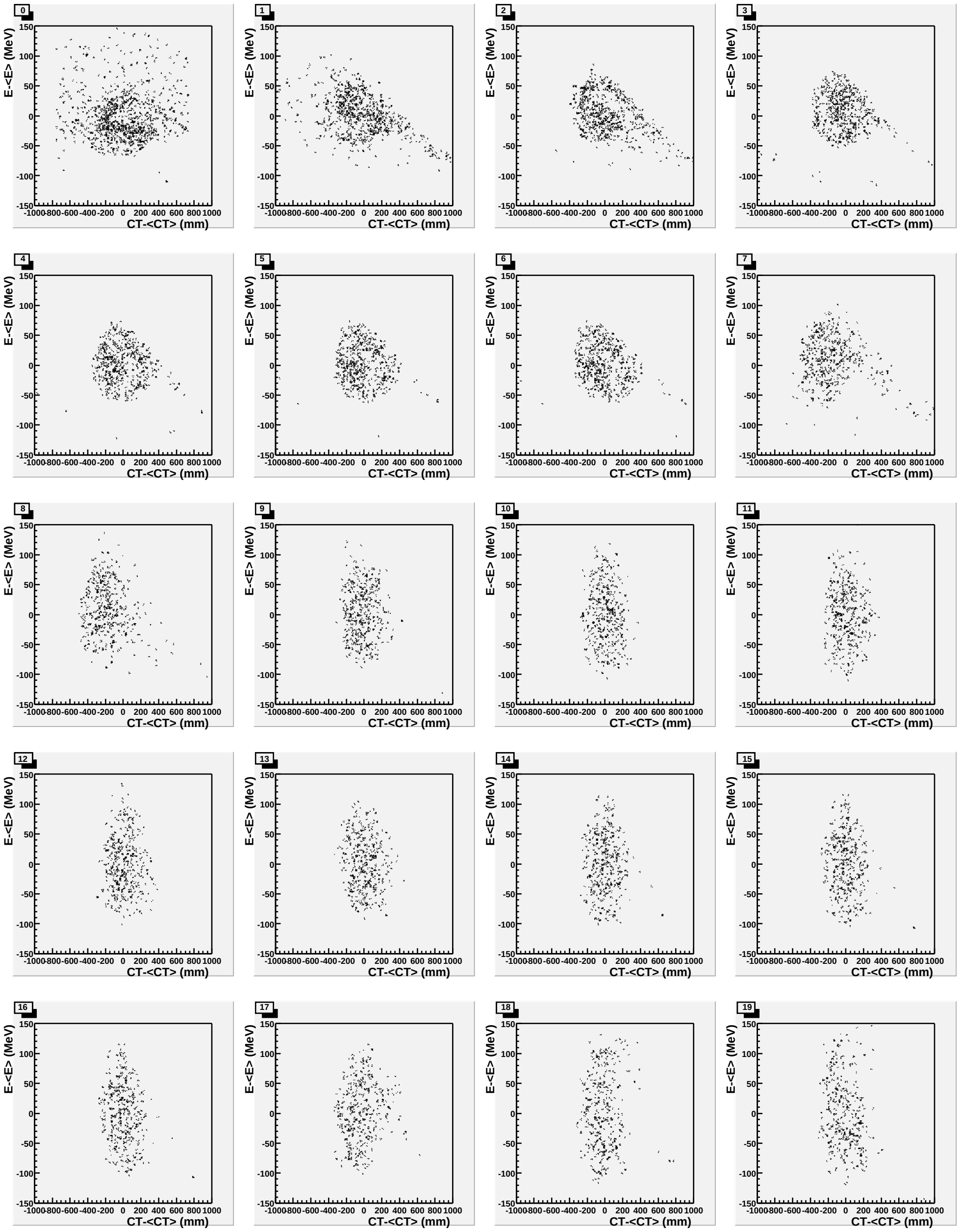

Figure B.23: Evolution of the longitudinal phase space. Plots 0 and 19 correspond to the initial and cooled beam, respectively. Plots 4, 5, and 6 (13, 14, 15) show the beam immediately before, in the middle, and after the first flip (second flip) region. The rest of the plots are snapshots of the beam taken approximately every five cooling cells.

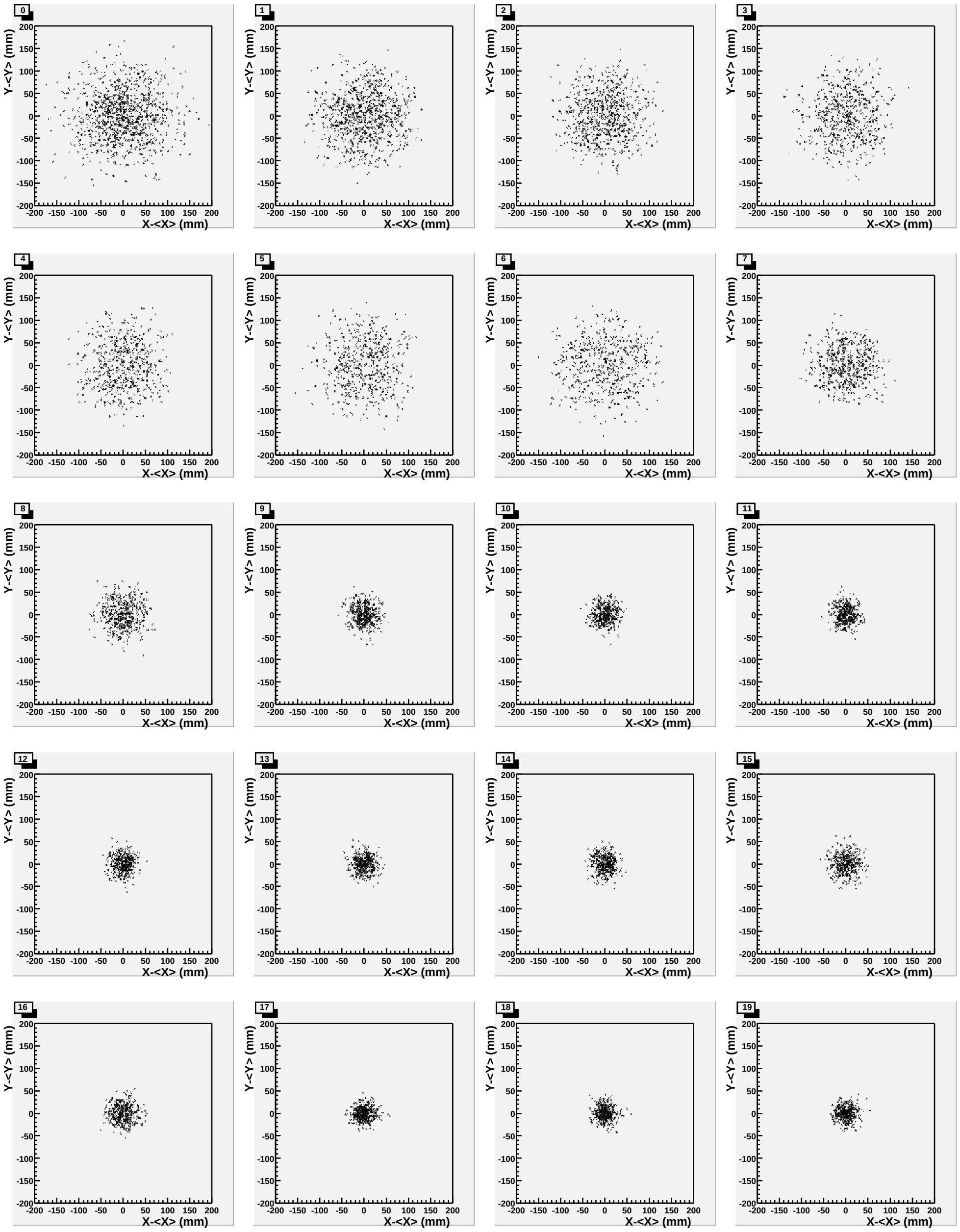

Figure B.24: Evolution of the beam size. Plots 0 and 19 correspond to the initial and cooled beam, respectively. Plots 4, 5, and 6 (13, 14, 15) show the beam immediately before, in the middle, and after the first flip (second flip) region. The rest of the plots are snapshots of the beam taken approximately every five cooling cells.

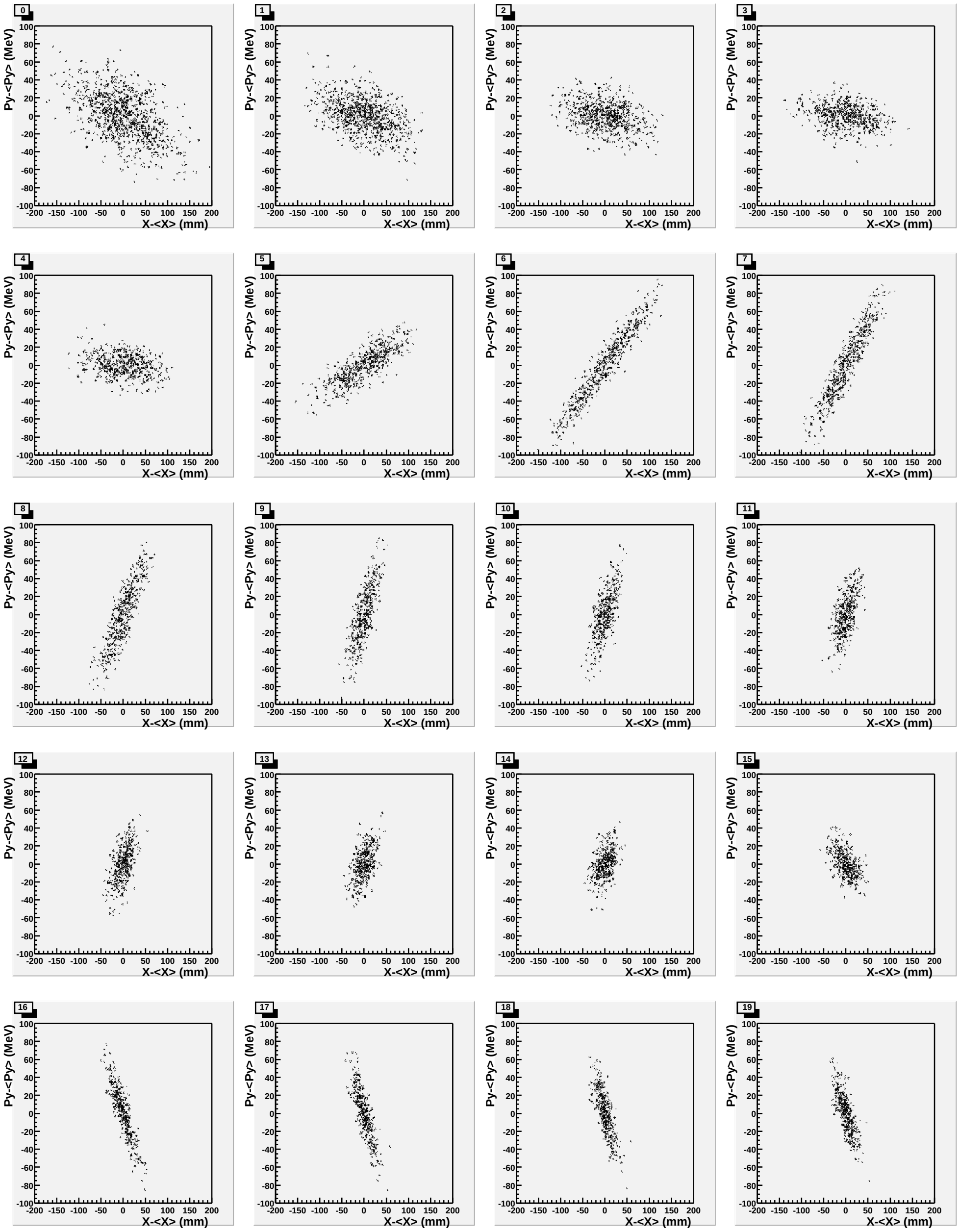

Figure B.25: Evolution of p_y versus x. Plots 0 and 19 correspond to the initial and cooled beam, respectively. Plots 4, 5, and 6 (13, 14, 15) show the beam immediately before, in the middle, and after the first flip (second flip) region. The rest of the plots are snapshots of the beam taken approximately every five cooling cells.

B.4.2.8 Muon/Proton (μ/p) Yield

The Muon/Proton Yield at the beginning of the cooling channel is 0.191, as listed in Table B.7. This means that at the end of the cooling channel, for the "realistic" beam with optimized window dimensions (b), the μ/p yield is 0.191 $\times$ transmission=0.076. If we upgraded the proton driver to 24 GeV, and the carbon target to a liquid mercury target (to match the baseline parameters set in the current feasibility study for a ν source), this yield should be scaled by a factor 24/16 $\times$ 1.9. The yield at the end of the DF cooling channel would therefore be $\simeq$0.22 muons per proton.

There are, however, constraints given by the acceptance associated with the accelerating system which follows the cooling channel: the linac, the recirculating linac, and the storage ring. A particle in a beam will be accepted by a succeeding accelerator if the following equations are satisfied:

$$\frac{\Delta z^2}{\beta_s \epsilon_z} + \frac{(\Delta p/p)^2 \beta_s}{\epsilon_z} < \frac{A_L}{\varepsilon_z}$$

$$\frac{\Delta r^2}{\beta_\perp \epsilon_x} + \frac{\Delta r'^2 \beta_\perp}{\epsilon_x} < \frac{A_\perp}{\varepsilon_x} ,$$

where $\Delta z = z - z_\circ$ and $\Delta p/p = (p - p_\circ)/p$, with z, p the particle z coordinate and total momentum, and $z_\circ$, $p_\circ$ the beam mean values for z and p. In the condition for the transverse direction, $\Delta r^2 = (x - x_\circ)^2 + (y - y_\circ)^2$ and $\Delta r' = \Delta p_T/p$, with p_T the particle transverse momentum; The longitudinal and transverse beta functions, β_s and $\beta_\perp$, are $\sigma_z/\sigma_{\Delta p/p}$ and $\sigma_x/\sigma_{x'}$, respectively. The normalized longitudinal and transverse emittance are invariant under Lorenz transformations. They are defined as:

$$\varepsilon_z = \beta\gamma\epsilon_z \ , \quad \epsilon_z = \sigma_z \sigma_{\Delta p/p}$$

$$\varepsilon_x = \beta\gamma\epsilon_x \ , \quad \epsilon_x = \sigma_x \sigma_{x'}$$

The longitudinal and transverse accelerator acceptances, A_L and $A_\perp$, depend on machine parameters. A_L also depends on the beam nominal energy which determines the vertical size of the r.f. bucket $(E - E_\circ)$.

In the previous chapters, the acceptance of the accelerator system following the cooling channel was set to $A_L = 150$ mm and $A_\perp = 15$ mm. These values correspond to a beam nominal momentum of 200 MeV/c, which is constant through the channel for the baseline SFOFO. Since the DF channel accelerates the beam to 308 MeV/c, it would also replace the first section of the post-cooling linac, which would have a larger bucket and, therefore, accept a beam with larger longitudinal emittance. Since the longitudinal acceptance for a linac is $A_L \propto p^{3/2}$, the longitudinal acceptance cut for the DF channel would be

A_L=150 mm×(308/200)$^{3/2}$=286 mm. The issue of whether the large momentum spread associated with the DF channel could be accepted by the recirculating linac and the storage ring is currently under investigation. Fig. B.26 shows the μ/p yield at the end of the DF cooling channel as a function of the longitudinal acceptance of the downstream system for different values of the normalized transverse acceptance cut. For A_L=150 mm (286 mm) and $A_\perp$=15 mm, the μ/p yield is 0.118 (0.176).

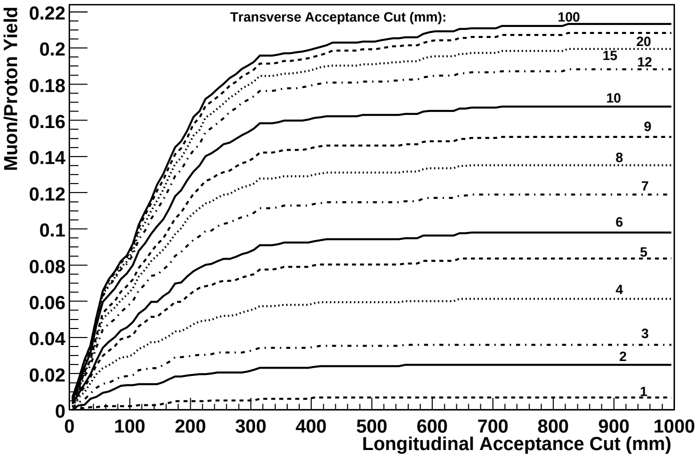

Figure B.26: μ/p yield at the end of the DF cooling channel as a function of the normalized longitudinal acceptance of the downstream system for different values of the normalized transverse acceptance cut. The optimum values of transverse and longitudinal acceptance are ∼15 mm and ∼300 mm, respectively. These acceptances are roughly consistent with those used for the baseline SFOFO cooling channel described in Chapter 5.

B.4.2.9 Summary

We have developed a conceptual and engineering design of a double flip cooling channel, and studied its performance tracking a "realistic" initial beam through a detailed GEANT4 simulation of the channel. The double flip channel offers greater mechanical simplicity than the baseline SFOFO, since it has only two field reversals. A final μ/p acceptance of 0.076 in the cooled beam is computed for a beam produced by a 16 GeV proton driver and a carbon target. If we upgraded the machine to a 24 GeV proton driver and a liquid mercury target, as in feasibility study II, the number of muons per proton would almost triple to 0.22. The acceptance cuts associated with the downstream accelerator further reduce this number following the curves in Fig B.26. The final transverse emittance of the beam before the acceptance cuts is 1.85 mm, which corresponds to a cooling factor of 6.8. The final longitudinal emittance before the acceptance cuts is 77.6 mm.

The current design can be further improved and optimized with modifications of the magnetic field strengths, r.f. parameters, section lengths, and window dimensions.

B.4.3 Emittance Exchange

In the baseline design, there is a large loss ($\approx 50\%$) of muons as they pass through the cooling channel. This is due mainly to the fact the lattice does not transport the increases in momentum spread that arise in the absorbers. This loss could be greatly reduced if the longitudinal acceptance of the lattice were increased, for instance by increasing the energy as the beam cools (as done in the double-flip alternative, see Section B.4). But this would not greatly improve the final result because the longitudinal acceptance is subsequently limited in the acceleration in particular, in the RLA. Increasing the acceptance there is expensive.

The preferred solution would be to cool the longitudinal emittance [14]. This can, in principle, be done by introducing dispersion (correlation of momentum with some transverse dimension) and placing a shaped absorber so that the higher momentum particles pass through more material than the lower momentum ones. In such a process, while the longitudinal emittance is reduced, the transverse emittance is increased, and thus we have emittance exchange, rather than cooling. When emittance exchange is combined with transverse cooling, however, all dimensions would be cooled.

This process, though simple in concept, has been found in full 6D simulations to be surprisingly hard to achieve efficiently. In unbunched beams, momentum spread can be efficiently exchanged with transverse emittance using bent solenoids or helical magnets. But in such systems, the dispersion introduces time-momentum correlations, that, for bunched beams in the presence of rf, greatly complicate the dynamics. Current designs do achieve some cooling in 6D, but with less than ideal efficiency. The problem will, we believe, be solved—it must be solved to realize a muon collider—and, when solved, could provide up to a factor of two improvement in performance. Further, if the cooled beam emittances could be further reduced, then the needed accelerator acceptances could be reduced, with concomitant cost savings.

B.4.4 NCRF: Grid of Tubes Alternative to Foil Windows.

Table B.11: Performance dependency on rf cavity apertures.

Maximum aperture (cm)	μ/p Be foil	μ/p Al tubes
21	.174	0.189
25	0.19	0.204
30	0.195	0.21

If the radii of the Be foil rf windows could be increased without increasing their thickness, then the performance can be improved. Table B.4.4 shows results for the baseline window thicknesses, and for 80μm Al windows that correspond in material thickness to a grid of tubes (see below). In both cases there appear to be significant gains. However, for edge-cooled Be foils, their thickness must be increased as the fourth power of radius to avoid excessive temperature rise. If this is done, the performance falls instead of rising. For a gas-cooled grid of thin-walled tubes, however, the pipe thickness is independent of aperture radius, and no degradation would be expected as the aperture increases.

Tracking with 5 cm diameter pipes has shown that the field non-uniformities lead to increases in emittance, but these problems can be avoided if the pipe diameter is reduced and the number of pipes is increased. A second advantage of many small tubes is that, for a given pressure, the wall thicknesses can be reduced.

For 1-cm diameter pipes, spaced on 2-cm centers, with wall thicknesses of 25 μm) the tension in the walls with 1 atmosphere of gas in the pipes would be only 3000 psi, which should be acceptable. For this diameter, the non-uniform field effects appear small. When a pair of such grids (at right angles to one another) is simulated by a plane foil with the same average material thickness (80 μm Al), then the performance gain with respect to the baseline, as seen in Table B.4.4, is 17% for a 25 cm aperture and approximately 20% for a 30 cm aperture (see Section 14.5 for a discussion of the grid tube approach).

B.5 Acceleration

B.5.1 Accelerator Acceptance.

The acceleration of the muons represents a major cost of the system. This cost could be reduced if the longitudinal and/or transverse acceptances could be reduced. And, conversely, the performance could be improved if these acceptances could be increased. The performance *vs.* acceptances are plotted in Fig. B.27. It is seen that a significant gain in performance could be achieved with greater transverse acceptance, but that the baseline longitudinal aperture already accepts almost all muons.

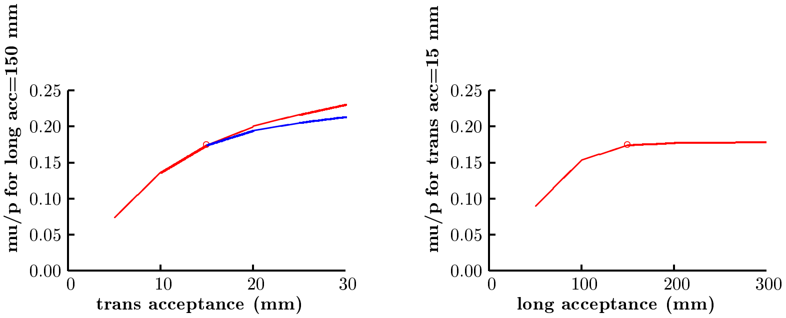

Figure B.27: Performance *vs.* accelerator acceptance: a) (left) transverse (upper line includes re-optimization of cooling length); b) (right) longitudinal. The baseline parameters are indicated by the circles.

B.5.2 Dogbone Configuration

A parametric study of costs [19] has been done on conventional racetrack and dogbone RLAs. The method used a semi-automatic longitudinal motion design, minimizing the energy spread. The costs were taken from the Feasibility Study-I: linac costs proportional to energy gain (C=35 ΔE per GeV) and arc costs proportional to length and energy spread (C=0.18 ΔE $\delta p/p$ per GeV and %.) The cost units are such that the two RLAs of Study-I cost 500 units.

For the conventional racetrack design (Fig. B.28,) the method shows that a cost minimum is achieved with 6 turns (Fig. B.30). However, four passes have been chosen for several practical reasons, including the difficulties of designing a switchyard with greater than 4 paths. If these problems could be overcome, then a cost saving of approximately 7% might be achieved.

An alternative geometry for the RLA is the dogbone (Fig. B.29). In this geometry there is only one linac, with the beam passing through it in alternate directions. Despite the larger number of passes, the number of paths on any one side of a switchyard is only

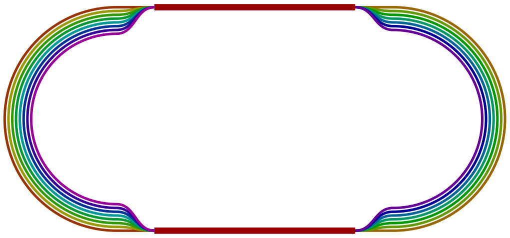

Figure B.28: Schematic of conventional racetrack RLA.

Figure B.29: Schematic of dogbone RLA.

four—no more than in the baseline. The savings in a dogbone arise primarily from the ability to reduce the length of the arcs when the momentum is lower. (If all the arcs were forced into a single tunnel, the gains would be lost.) A serious study based on actual costs will be needed to quantify the benefits of alternative accelerator approaches. This should include the use of FFAG (Fixed-Field Alternating Gradient) rings. However, the main motivation for an FFAG, its large longitudinal acceptance, seems moot based on Fig. B.27.

B.6 Detector

B.6.1 Introduction

An alternate to WIPP [20] for the location of the long-baseline neutrino detector is the Soudan Mine in northern Minnesota.

The Soudan Site is located in the Soudan Mine State Park, Minnesota; it has been the location of an underground neutrino facility since 1984 and is currently being prepared for the installation of the MINOS [21] experiment, which is scheduled to start taking data

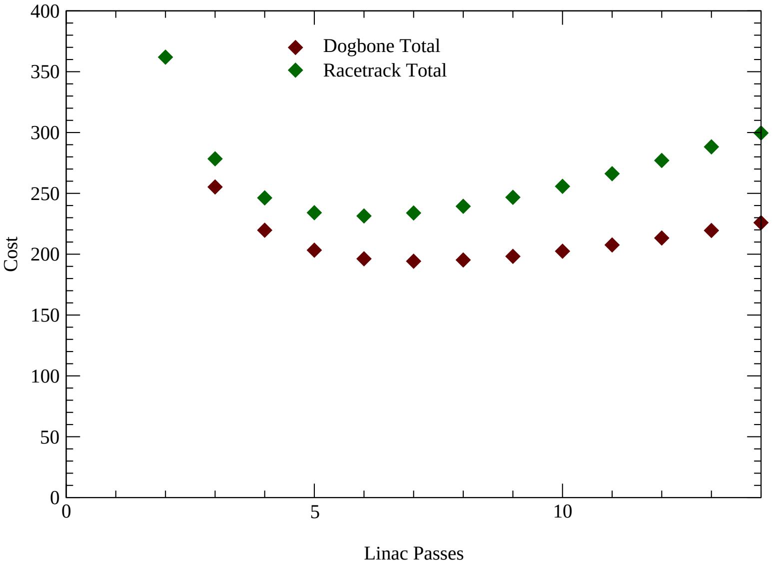

Figure B.30: Relative costs of RLA's *vs.* number of passes.

in 2004.

The Soudan site has both advantages and disadvantages compared with WIPP. The advantages include closer distance to BNL, higher event rate, existing infrastructure, and an operating underground neutrino detector. The closer distance means that the storage ring at the Neutrino Factory can have a smaller inclination angle (7.7° Soudan *vs.* 13.1° WIPP) which translates into easier and less expensive civil engineering. The 1700 km location also means a higher neutrino rate per kton at Soudan than at WIPP. A detector at Soudan could be 1/3 the size of one at WIPP and still have the same number of ν-interactions/year (see Table B.12.)

The site has infrastructure well matched to the requirements of a physics experiment, and offers the potential to use an existing detector (MINOS) upgraded for the Neutrino Factory program. The closer distance to BNL is also a disadvantage of the Soudan site. At 1700 km, both the matter oscillation and the CP violating term, δ, are harder to observe (See Fig. 15.1). However, the measurement of θ_{13} and the improvement in both $\Delta m_{23}{}^2$ and θ_{23} should not be significantly affected by the shorter distance.

Table B.12: Event rates at possible detectors at Soudan and WIPP.

E_μ Muon Ring (GeV)	Baseline (km)	E_{ν_μ}	E_{ν_e}	$N(\nu_\mu$ CC) (per kton-year)	$N(\nu_e$ CC) (per kton-year)
$10_{\text{BNL-SOU}}$	1700	7.5	6.5	260	120
$20_{\text{BNL-SOU}}$	1700	15	13	2150	960
$20_{\text{BNL-WIPP}}$	2900	15	13	740	330

B.6.2 Site

As noted the Soudan Site has two excavated halls available for physics experiments: the MINOS hall and a neighboring hall in which Soudan II was located. The halls are not optimally oriented with respect to BNL. MINOS is rotated 39° with respect to a ν-beam incident from Brookhaven. The second hall is also pointed away from BNL at a significant angle, but may be wide enough to allow for the installation of a detector rotated in an appropriate direction for the Neutrino Factory. Services such as elevator access, electricity, water and cranes, though available in both halls, would presumably need to be upgraded if a larger experiment were installed.

B.6.3 Detector

The MINOS detector could be upgraded to increase its mass for a future experiment at the Neutrino Factory. MINOS is a 5 kton detector composed of layers of 4-cm steel absorber plates interleaved with layers of scintillator slats (Fig. B.32). There is a field coil that runs through the center of each plate down the length of the detector. The coil magnetizes the plates, producing a toroidal field with a field of 1.5 T. The MINOS detector operates similarly to the Steel/Scintillator/PDT detector described in Chapter 15. The magnetic field enables the identification of the sign of the leading muon resulting from ν CC interactions. The momentum and energy of the muon can be determined by a combination of bending in the $\vec{B}$-field and range. Background events are rejected through momentum and isolation cuts, range-out and timing. The MINOS detector is approximately 40% steel by volume. The thin steel plates give the experiment the ability to identify muons down to 1 GeV/c and to possibly measure ν_e events. An upgrade to MINOS would add a front section to the detector that was 80% steel by volume, including 20-cm thick magnetized-steel absorber plates interleaved with standard MINOS scintillator slats. This could allow the detector to approach a total mass of 15 kton. Such an upgrade would totally fill the available space in the MINOS hall, and would not resolve the issue of

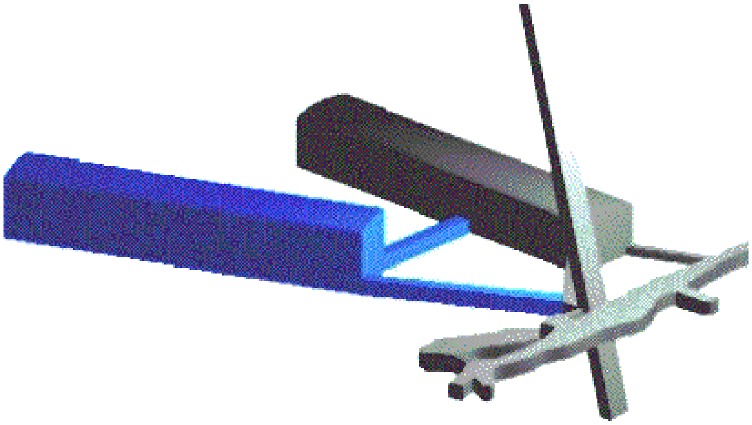

Figure B.31: The Soudan Site. The two underground experimental halls are located at 714 m below the surface. The MINOS hall is on the left and the Soudan II hall is on the right.

the detector angle relative to the incident beam angle. An alternate solution would be to build a 15 kton detector in the second hall available at Soudan. The second hall is wider than the MINOS hall, and could accommodate a detector installed at an angle rotated toward BNL. With this solution, the angle between the detector's major axis and the neutrino beam would be smaller, though not 0°. The choice between these alternate solutions requires additional study.

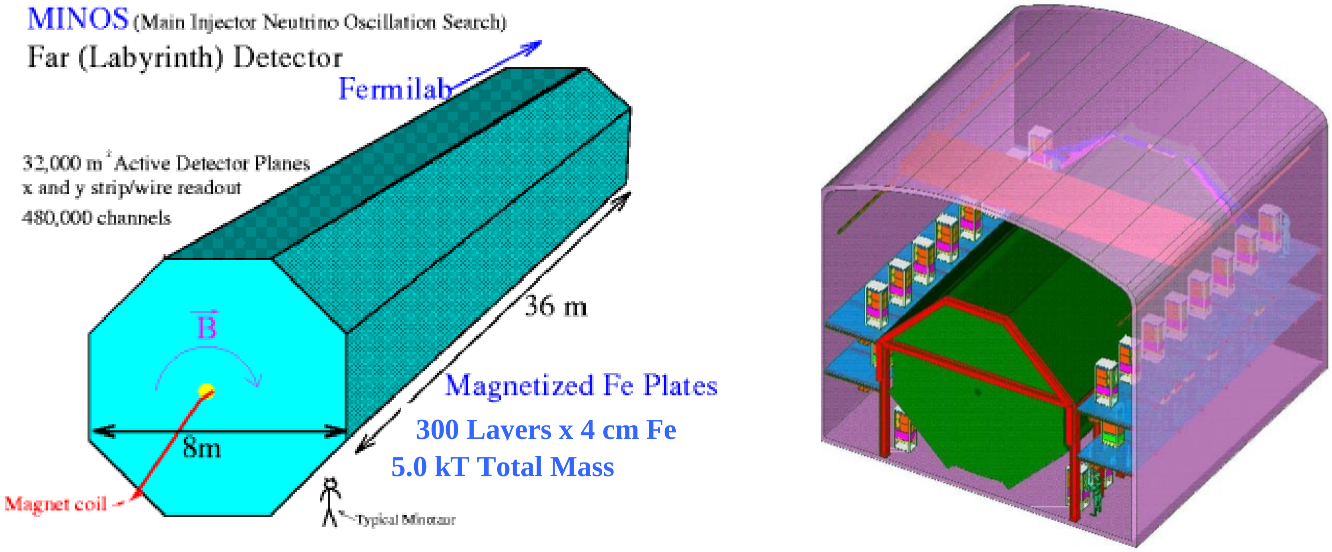

Figure B.32: Two views of the Minos detector showing both its general features and its configuration in the experiment hall.

B.6. Detector

Bibliography

[1] *A Cupronickel Rotating Band Pion Production Target for Muon Colliders*, B.J. King *et al.*, Proc. PAC'99, IEEE, pp. 3041-3.

[2] *Rotating Band Pion Production Targets for Muon Colliders and Neutrino Factories*, B.J. King, NIM A 451 (2000) pp. 335-343, Proc. ICFA/ECFA Workshop "Neutrino Factories based on Muon Storage Rings (nuFACT'99)", physics/0005007.

[3] *Some thoughts on a high-power, radiation cooled, rotating toroidal target for neutrino production*, J.R.J. Bennett, NIM A 451 (2000) pp. 344-348, Proc. ICFA/ECFA Workshop "Neutrino Factories based on Muon Storage Rings (nuFACT'99)".

[4] *A Rotating Band Target for Pion Production at a Neutrino Factory, using Study II Parameters*, B.J. King, N.V. Mokhov, N. Simos and R.J. Weggel, Muon Collider Note 199,
http://www-mucool.fnal.gov/notes/notes.html.

[5] BNL g-2 Collaboration, *The BNL Muon Storage Ring Beamline*, to be published.

[6] Graphalloys are manufactured from molded graphite impregnated with metal. Graphalloy is a registered trademark of the Graphite Metallizing Corporation.

[7] N.V. Mokhov, "The MARS Code System User's Guide", Fermilab-FN-628 (1995). N.V. Mokhov and O.E. Krivosheev, "MARS Code Status", Fermilab-Conf-00/181 (2000). http://www-ap.fnal.gov/MARS/ .

[8] N. Holtkamp, D. Finley, Editors, *A Feasibility Study of a Neutrino Factory Based on a Muon Storage Ring*, Aug., 2000 (http://www.fnal.gov/projects/muon_collider/nu-factory/fermi_study_after_april1st/)

[9] P. Sievers, *A Stationary Target for the CERN Neutrino Factory*, presented at NUFACT01, Tsukuba, Japan

{http://www-prism.kek.jp/nufact01/May26/WG3/26wg3_sievers.pdf}

[10] R.B. Palmer, C. Johnson and E. Keil, *A Cost-Effective Design for a Neutrino Factory*, BNL-66971, CERN SL/99-070 AP, NEUTRINO FACTORY NOTE 09; published in the Proceedings of NuFact99, Lyon, (http://lyopsr.in2p3.fr/nufact99/.)

[11] N. Marseille and W. Pirkl, *Sparking Cavity Test Report*, {http://nicewww.cern.ch/~molat/neutrino/nf52.pdf}

[12] D. Neuffer "High Frequency Buncher and $\phi - \delta E$ Rotation for the $\mu^+ - \mu^-$ Source", MUCOOL Note 0181, Oct. 2000, (http://www-mucool.fnal.gov/notes/)

[13] V. Balbekov, P. Lebrun, J. Monroe, P. Spentzouris, *The Single Field Flip Cooling Channel for a Neutrino Factory*; MUC Note 0125, March 2000, (http://www-mucool.fnal.gov/notes/)

[14] G. Hanson, (http://needmore.physics.indiana.edu/~gail/emittance_exchange.html)

[15] V. Balbekov, *Double Field Flip Cooling Channel for Neutrino Factory (front-end simulation)*, MuCool #118, April 2000.

[16] *A Feasibility Study of a Neutrino Source Based on a Muon Storage Ring.* Edited by N. Holtkamp and D. Finley, March 2000.

[17] HTTP://WWWINFO.CERN.CH/ASD/GEANT4/GEANT4.HTML

[18] Open Inventor. Registered trademark of Silicon Graphics Inc.

[19] S.J. Berg, unpublished (http://pubweb.bnl.gov/people/jsberg/talks/010131/0101310all.pdf); J.S. Berg, et al., *Acceleration Stages for a Muon Collider*, Proc. PAC99, New York (1999), pp. 3152.

[20] The WIPP Home Web Page, *http://www.wipp.carlsbad.nm.us/wipp.htm*

[21] The MINOS Experiment and the NuMI beam line, *http://www-numi.fnal.gov:8875/*